AGU PUBLICATIONS

JGR

Journal of Geophysical Research: Earth Surface

RESEARCH ARTICLE
10.1002/2014JF003410

Key Points:
- Tectonic processes determine first-order denudation rates in the Arun but are modulated by climate
- Local geomorphic processes impact 10Be concentrations in river sands even in large basins
- Downstream fining causes upstream areas of large basins to be excluded from distal sediment samples

Supporting Information:
- Text S1 and Figures S1–S4
- Tables S1–S3

Correspondence to:
S. M. Olen,
olen@geo.uni-potsdam.de

Citation:
Olen, S. M., B. Bookhagen, B. Hoffmann, D. Sachse, D. P. Adhikari, and M. R. Strecker (2015), Understanding erosion rates in the Himalayan orogen: A case study from the Arun Valley, *J. Geophys. Res. Earth Surf.*, *120*, 2080–2102, doi:10.1002/2014JF003410.

Received 8 DEC 2014
Accepted 28 AUG 2015
Accepted article online 3 SEP 2015
Published online 15 OCT 2015

Understanding erosion rates in the Himalayan orogen: A case study from the Arun Valley

Stephanie M. Olen[1], Bodo Bookhagen[1], Bernd Hoffmann[1], Dirk Sachse[1,2], D. P. Adhikari[3], and Manfred R. Strecker[1]

[1]Institute of Earth and Environmental Science, University of Potsdam, Potsdam, Germany, [2]GFZ German Research Centre for Geosciences, Section 5.1 Geomorphology, Helmholtz Centre Potsdam, Potsdam, Germany, [3]Department of Geology, Tribhuvan University, Kathmandu, Nepal

Abstract Understanding the rates and pattern of erosion is a key aspect of deciphering the impacts of climate and tectonics on landscape evolution. Denudation rates derived from terrestrial cosmogenic nuclides (TCNs) are commonly used to quantify erosion and bridge tectonic (Myr) and climatic (up to several kiloyears) time scales. However, how the processes of erosion in active orogens are ultimately reflected in ^{10}Be TCN samples remains a topic of discussion. We investigate this problem in the Arun Valley of eastern Nepal with 34 new ^{10}Be-derived catchment-mean denudation rates. The Arun Valley is characterized by steep north-south gradients in topography and climate. Locally, denudation rates increase northward, from $<0.2\,\mathrm{mm\,yr^{-1}}$ to $\sim1.5\,\mathrm{mm\,yr^{-1}}$ in tributary samples, while main stem samples appear to increase downstream from $\sim0.2\,\mathrm{mm\,yr^{-1}}$ at the border with Tibet to $0.91\,\mathrm{mm\,yr^{-1}}$ in the foreland. Denudation rates most strongly correlate with normalized channel steepness ($R^2 = 0.67$), which has been commonly interpreted to indicate tectonic activity. Significant downstream decrease of ^{10}Be concentration in the main stem Arun suggests that upstream sediment grains are fining to the point that they are operationally excluded from the processed sample. This results in ^{10}Be concentrations and denudation rates that do not uniformly represent the upstream catchment area. We observe strong impacts on ^{10}Be concentrations from local, nonfluvial geomorphic processes, such as glaciation and landsliding coinciding with areas of peak rainfall rates, pointing toward climatic modulation of predominantly tectonically driven denudation rates.

1. Introduction

Denudation, the removal of mass from the landscape, is the combined result of tectonic forces that expose rock at the surface and climatic forces that provide the erosive agents to remove it. An effort to understand the relationship between the rates of denudation and the tectonic and/or climatic forces that drive denudation has been a main undertaking in Earth science in recent decades. Many theoretical and field studies have suggested a close link between climate and denudation rates in a variety of geodynamic settings [e.g., *Reiners et al.*, 2003; *Hales and Roering*, 2005; *Roe et al.*, 2008; *Moon et al.*, 2011; *Bookhagen and Strecker*, 2012; *Ferrier et al.*, 2013a, 2013b; *Herman et al.*, 2013], ultimately resulting in characteristic landscapes in accord with climatic zonation [e.g., *Büdel*, 1982]. In contrast, another group of studies has argued against a strong climatic influence on denudation rates in many orogens and emphasizes a more decisive role of tectonic processes in landscape evolution [e.g., *Riebe et al.*, 2001, 2004; *Burbank et al.*, 2003; *Safran et al.*, 2005; *Willenbring and von Blanckenburg*, 2010; *Godard et al.*, 2014; *Scherler et al.*, 2014]. However, the time scales of these studies differ significantly, from tens (e.g., suspended sediment flux) to millions (e.g., thermochronometry) of years.

Over the last quarter century, the assessment of erosion processes using terrestrial cosmogenic nuclides (TCNs) has been increasingly refined as a widely used method in geomorphology due to its ability to quantify catchment-mean denudation rates on 10^2–10^5 year time scales, thus bridging the gap between instrumentally recorded erosion rates and rates obtained from thermochronology and the stratigraphic records of geologic archives [*Bierman and Steig*, 1996; *Brown et al.*, 1995; *Granger et al.*, 1996; *von Blanckenburg*, 2005; *Granger et al.*, 2013]. Several studies have used ^{10}Be concentrations in detrital sand samples to investigate how climate and/or tectonics influence denudation rates in mountain belts around the world [e.g., *Safran et al.*, 2005; *Bookhagen and Strecker*, 2012; *Godard et al.*, 2014; *Scherler et al.*, 2014]. However, the assumptions necessary to calculate catchment-mean denudation rates from a detrital river sand sample are frequently violated in climatically very dynamic, active tectonic environments, and the extent to which ^{10}Be

concentrations reflect actual denudation rates is still under debate [e.g., *Lupker et al.*, 2012; *McPhillips et al.*, 2014; *Puchol et al.*, 2014].

Because it has been proposed as a location where tectonic-climate coupling might occur [e.g., *Molnar and England*, 1990; *Hodges et al.*, 2004; *Thiede et al.*, 2005; *Huntington et al.*, 2006; *Hirschmiller et al.*, 2014], the Himalaya represents an area where understanding denudation rates is of great scientific importance. The highest mountain range in the world, the Himalaya is rapidly and actively uplifting and eroding [e.g., *Molnar and Tapponnier*, 1975; *Avouac*, 2003] and is characterized by an extreme and highly seasonal climate. The Indian summer monsoon (ISM) delivers large amounts of rainfall to the Himalaya, focused along the southern orographic front due to high topographic barriers [*Bookhagen and Burbank*, 2006; *Bookhagen and Burbank*, 2010]. Monsoonal rainfall drives large discharge events and sediment fluxes toward the Indo-Gangetic foreland [*Wulf et al.*, 2010, 2012] and eventually into submarine fans and beyond [*Milliman and Syvitski*, 1992; *Clift et al.*, 2001; *Curray et al.*, 2002]. Authors of recent studies of ^{10}Be TCN from the Himalaya have argued, however, that climate does not play a decisive role in driving denudation rates, which are instead controlled principally by tectonic deformation and uplift [e.g., *Godard et al.*, 2014; *Scherler et al.*, 2014].

The impact of climate on sediment flux and topography through variability of the ISM may have been stronger in the past [e.g., *Goodbred and Kuehl*, 2000; *Bookhagen et al.*, 2005b]. Evidence exists for a stronger ISM in the early Holocene and a relatively weak ISM during the Last Glacial Maximum and the present day [e.g., *Prins and Postma*, 2000; *Thamban et al.*, 2002; *Fleitmann et al.*, 2003; *Bray and Stokes*, 2004; *Zhisheng et al.*, 2011]. The early Holocene intensified monsoon was associated with a twofold increase in sediment discharge to the Ganges-Brahmaputra fan [*Goodbred and Kuehl*, 2000], frequent large landslides in the orogen interior, and overall increased sediment flux in the NW Himalaya [*Bookhagen et al.*, 2005b]. Such studies document the sensitivity of the Himalayan system to changes in regional climate and the surface-process regime.

In this study, we present 34 new ^{10}Be TCN catchment-mean denudation rates from the Arun Valley in eastern Nepal to understand how climatic and tectonic processes affect ^{10}Be TCN concentrations and the resulting denudation rate calculations. The north-south flowing Arun is the fourth largest trans-Himalayan river and traverses the orogen through a deeply incised, narrow gorge (Figure 1). The Arun Valley is characterized by steep topographic and climatic gradients perpendicular to the strike of the Himalaya. These distinct gradients allow for a robust analysis of different climatic and topographic factors that may influence ^{10}Be concentration in river sand samples and possibly control regional denudation rates.

2. Background

2.1. Climatic Setting

Every year the ISM system delivers heavy, seasonal rainfall to the Himalaya as the Intertropical Convergence Zone migrates northward during the boreal summer [*Charney*, 1969; *Gadgil*, 2003]. The orographic barrier of the Himalaya focuses monsoonal rainfall along its southern flank, where mean annual rainfall locally exceeds 5 m yr^{-1} (Figure 1c) [*Bookhagen and Burbank*, 2010]. The Arun Valley is located relatively close to the Bay of Bengal (Figures 1b and 1c) and thus the main ISM moisture source. Weather stations maintained by the Nepal Department of Hydrology and Meteorology in the Arun record approximately 60% of annual rainfall during the peak ISM months (June through September); 80–90% of annual rainfall occurs from May to October [cf. *Bookhagen and Burbank*, 2010]. Because of the deeply incised, N-S oriented gorge, moisture is funneled through the Arun Valley northward into Tibet, resulting in greater rainfall in the upper sectors of the valley than on the surrounding higher-elevation areas (Figure 1c). Winter precipitation is primarily focused in the high-altitude regions [*Bookhagen and Burbank*, 2010; *Wulf et al.*, 2010], and snowfall is common in these areas [*Carpenter and Zomer*, 1996]. Reliable snowfall data from gauging stations, however, are not available in the Arun region as weather stations are principally located at low elevations not affected by snowfall. *Bookhagen and Burbank* [2010] calculated the snowmelt contribution of major Himalayan rivers across the Himalayan orogen and found that approximately 25% of total discharge in the Arun is related to snowmelt, as opposed to over 50% in the Western Himalaya.

2.2. Geologic and Tectonic Setting

Originating in Tibet, the Arun flows southward through the Himalayan orogen before joining the Sapt Kosi and the Ganges Rivers in the foreland. The course of the river exposes a natural cross section through the mountain belt: from the sedimentary Tethyan series in Tibet, through the Greater or High Himalayan Crystalline (HHC), the

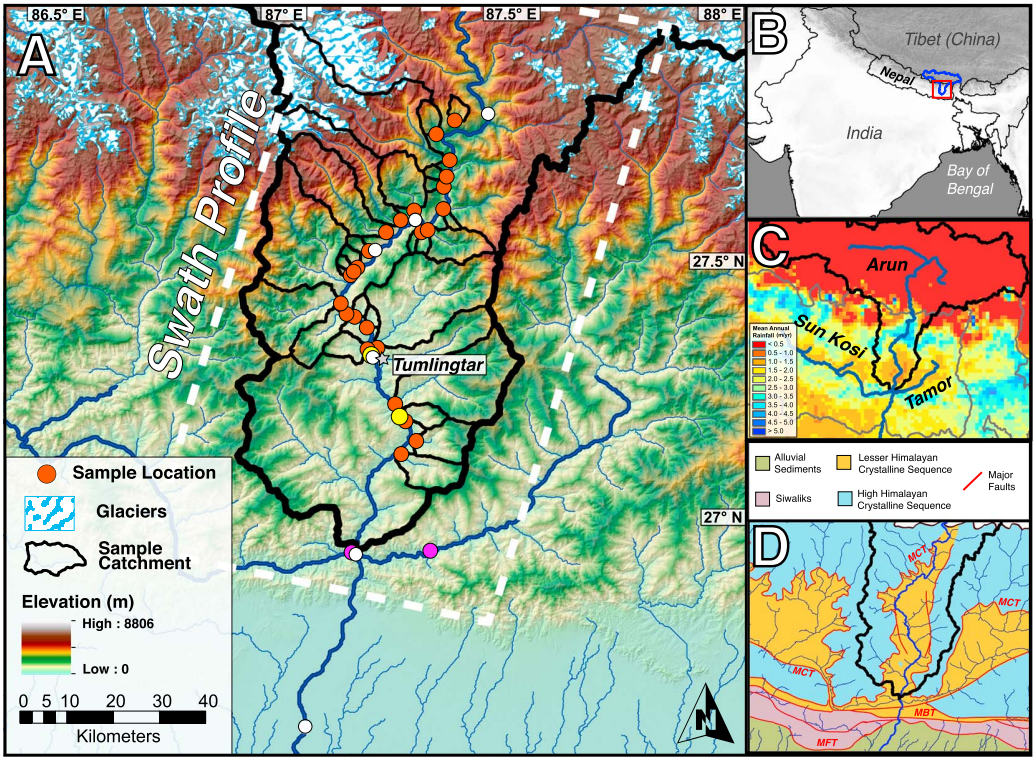

Figure 1. Overview of study area in the Arun Valley, eastern Nepal. (a) Map of study area showing elevation from SRTM 90 m DEM, river network (dark blue), and glaciers from GLIMS glacier database (light blue/white) [*GLIMS and National Snow and Ice Data Center*, 2005; http://www.glims.org/]. Sample locations of ^{10}Be TCN sample sites for tributaries (red) are shown with associated watersheds outlined (black); along with main stem (white), Sun Kosi and Tamor Rivers (pink), and fluvial fill terrace (yellow) sample locations (cf. Table 1). Downstream of the confluence of the Arun, Sun Kosi, and Tamor Rivers, the river is called the Sapt Kosi. The main stem Arun watershed is shown by a thick black outline. The swath area used for Figure 3 is shown in dashed white lines. (b) The Arun Valley in the regional context, including area from Figure 1a (red), and the entire Arun watershed, including area in Tibet (blue). (c) Mean annual rainfall (mm yr^{-1}) from calibrated TRMM 2B31 [*Bookhagen and Burbank*, 2010] showing double bands of high rainfall at the orographic fronts of the LH and HH and Sapt Kosi River network, including Arun, Sun Kosi, and Tamor (dark blue) and Arun watershed (black). Political boundaries are shown in gray for reference. (d) Geologic map of the study area after *Grujic et al.* [2011] showing major Himalayan lithologies and faults of eastern Nepal. MFT denotes Main Frontal Thrust, MBT Main Boundary Thrust, and MCT Main Central Thrust. Outline of the Arun watershed is shown in black.

Lesser Himalayan Crystalline (LHC), the Siwaliks, and finally to the alluvial plains of the Gangetic foreland [*Schelling*, 1992; *Grujic et al.*, 2011]. An aerially extensive tectonic window, identified by *Meier and Hiltner* [1993] as the Arun Tectonic Window, exposes LHC rocks below the Main Central Thrust (MCT) along the course of the Arun (Figure 1d). The northern extent of this window and the location of the MCT are poorly constrained [e.g., *Schelling*, 1992]. The Arun Tectonic Window corresponds to a large anticline [*Wager*, 1937], which *Montgomery and Stolar* [2006] suggested to result from focused bedrock incision of the Arun.

The lithology in the study area is dominated by crystalline metamorphic rocks, principally from the HHC and LHC. The LHC units in the Arun Valley, as mapped by *Schelling* [1992], are metasediments (e.g., metaquartzite, slate, phyllite, and metagraywacke) and augengneiss. HHC units are comprised of migmatites, paragneiss, and granites. No extensive carbonate or volcanic deposits are exposed, and all mapped lithologic groups are predominantly quartz-bearing. Because the Arun Tectonic Window follows the Arun Valley northward, we do not observe discrete variations in lithology perpendicular to strike within our study area (Figure 1d and Figure 2).

2.3. Geomorphic Setting

As it drains the Himalaya, the Arun displays a steep, graded channel profile in a narrow valley (Figure 2). Two large slope-break knickzones north of the Arun gorge, approximately corresponding to the location of the Southern Tibetan Detachment (STD), separate the Himalayan Arun from the Tibetan section of the river,

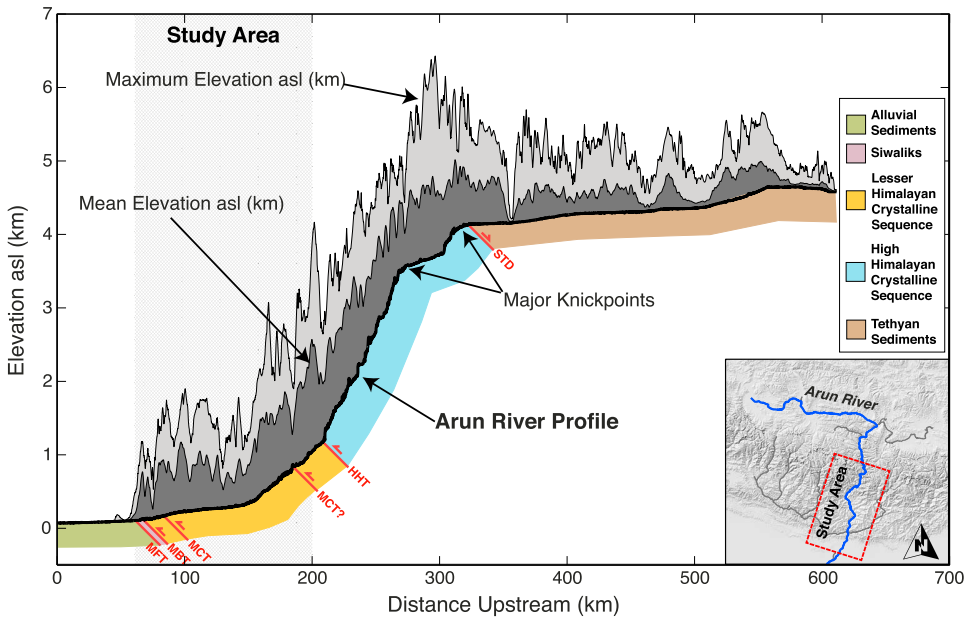

Figure 2. Longitudinal profile of Arun River from the Ganges Plain in the south to its source in southern Tibet. The river profile (black) is shown with mean elevation (dark gray) and maximum elevation (light gray) from a 1.5 km swath centered along the course of the river. The two large knickzones are easily visible in the river profile, as well as the transition from a steep graded profile ($\theta = 0.45$) to shallow profile ($\theta = 0.79$) downstream and upstream of the knickzones, respectively. Surface lithology along the Arun River after *Grujic et al.* [2011]; major fault locations after *Schelling* [1992] and *Grujic et al.* [2011]. The study area is shown in hatched gray. Inset shows map view of the region, with the Arun trunk stream highlighted in blue.

known locally as the Pum Qu. Similar knickzones of tectonic origin are observed in many trans-Himalayan rivers along strike [e.g., *Seeber and Gornitz*, 1983]. Above these knickzones the river has a shallow profile for the remainder of its upstream course and a broad, flat valley. Several fluvial fill terraces in the lower and middle reaches of the Arun have been mapped by *Lavé and Avouac* [2001], but few are preserved in the upper reaches of the valley. We observed several strath terraces and hanging valleys, particularly in the upper sections of our study area approaching the Tibetan border.

The topography of the Arun Valley is comprised of three principal topographic sectors (Figure 3a): the Lesser Himalaya (LH), with an average elevation of ~2 km above sea level (asl) and a mean hillslope angle of ~20°; the Higher Himalaya (HH), where mean elevation rises above 4 km asl and peaks are in excess of 8 km asl, with a mean hillslope angle of ~30°; and a topographic transition zone between the Lesser and Higher Himalaya, first identified in other areas along strike of the mountain belt as the Physiographic Transition Zone (PT_2) [*Hodges et al.*, 2001], marking a sharp break in topography.

In the Higher Himalaya, the Arun Valley hosts several glaciers [*Global Land Ice Measurements from Space (GLIMS) and National Snow and Ice Data Center*, 2005; http://www.glims.org/]. Larger valley glaciers are predominantly in western tributaries of the Arun. To the east, several small cirque glaciers exist in the Ama Drime and Higher Himalaya, but no large valley glaciers currently occupy these watersheds. In the Nepalese section of the Arun Valley, cirque and valley glaciers exist in the upper reaches of the northernmost tributaries flowing into the Arun, but are less prominent than on the northern flanks of the Higher Himalaya, where extensive glaciation extends down from the northern slopes of the Sagarmatha/Mount Everest and Makalu regions. Valley morphology suggests that past glaciation was more extensive in medium to large high-altitude tributaries, but there is no evidence of glaciers reaching the main stem Arun.

3. Methods

3.1. Climatic Data and Analysis

Rainfall in the Arun Valley was characterized using remotely sensed data from the Tropical Rainfall Measurement Mission (TRMM). We used the calibrated 12 year average mean annual rainfall product

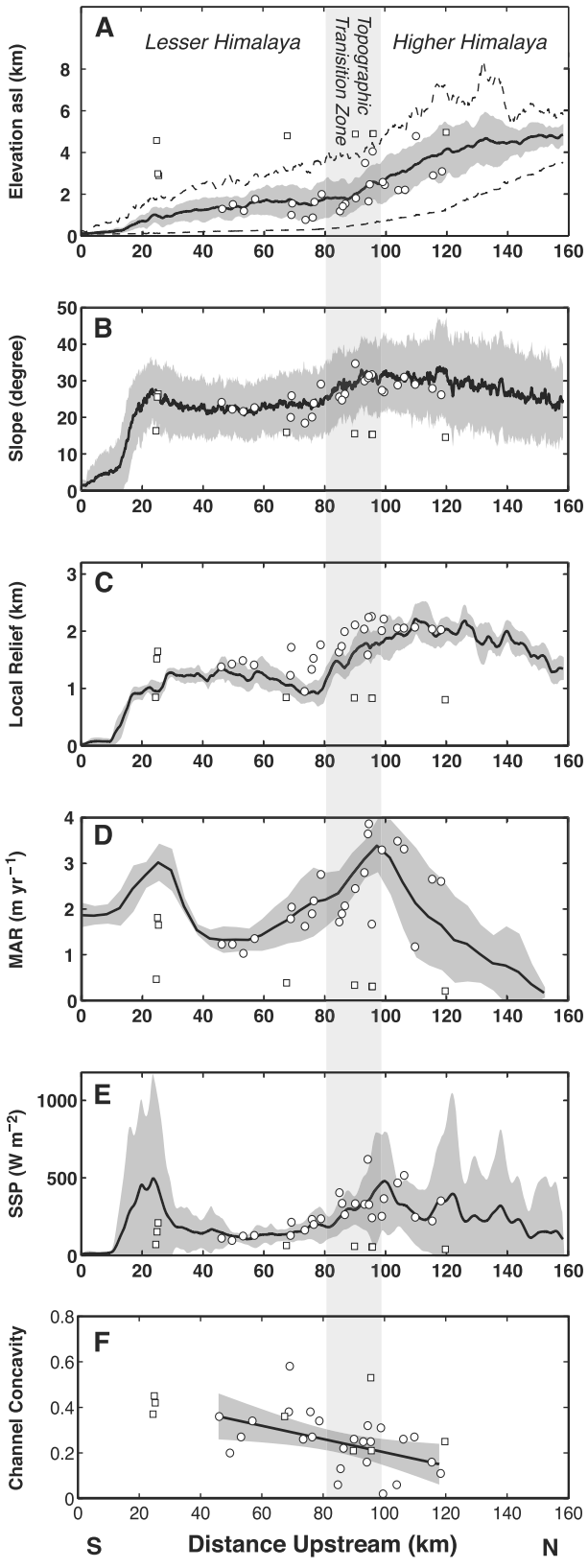

TRMM 2B31 [*Bookhagen and Burbank*, 2010] with a nominal spatial resolution of 5 × 5 km. Additionally, we used the National Snow and Ice Data Center (NSIDC) Global Land Ice Measurements from Space (GLIMS) database to define the location of present-day glaciers within our study area [*GLIMS and National Snow and Ice Data Center*, 2005; http://www.glims.org/]. Due to insufficient data, we do not account for snowfall or glacial melt in any of our climate-based analysis. Because of this, we acknowledge that metrics that depend on stream discharge, such as specific stream power (below), may be underestimated in high-altitude catchments affected by snowfall.

We calculated specific stream power (SSP), a measure of potential stream energy per unit area based on the stream power model [e.g., *Whipple and Tucker*, 1999; *Lague*, 2014], following Bookhagen and Strecker [*Bookhagen and Strecker*, 2012]. SSP (ω, W m^{-2}) incorporates climatic and topographic factors, such that

$$\omega = \frac{\gamma \times Q \times S}{w} \quad (1)$$

where γ is the specific weight of water (9819 N m^{-3}), Q is discharge (m^3 s^{-1}), S is the local bed slope (m m^{-1}), and w is the width of the channel (m). To account for the large spatial variations in rainfall in the Arun Valley, and therefore presumably runoff, we determined discharge based on

Figure 3. Swath profiles (from swath area in Figure 1) of (a) elevation, with Lesser Himalaya, topographic transition zone (shaded gray), and Higher Himalaya denoted; (b) slope; (c) 3 km radius relief; (d) mean annual rainfall [*Bookhagen and Burbank*, 2010]; (e) TRMM-weighted specific stream power (SSP); and (f) channel concavity from χ analysis for each sampled tributary and main stem location. Values are averaged across a 75 km wide swath area, chosen to include all major tributaries to the Arun River in our study area. Mean swath values are shown in black with ±1σ in shaded gray. Catchment-mean values from all sampled tributaries (circles) and main stem locations (squares) are shown along swath. Concavity values (*F*) are shown with linear regression of tributary concavity values and upstream distance; the shaded gray region represents the 95% confidence bounds. The topographic transition zone is shown in all panels by the light gray bar.

both upstream area and TRMM-derived rainfall. We calculated SSP for every 90 m pixel in the digital elevation model (DEM) and have used an 11-pixel (~1 km) moving average channel-slope filter to remove outliers. SSP values were explicitly calculated from channel slopes. Channel width was defined using a simple scaling model, such that channel width was assumed to increase proportionately to discharge, following a power law relationship with an exponent of 0.4 [*Knighton*, 1999; *Whipple*, 2004; *Craddock et al*., 2007].

3.2. Topographic and Geologic Data and Analysis

Topographic analysis was performed on the 90 m resolution Shuttle Radar Topography Mission (SRTM) digital elevation model (DEM) v4.1 provided by Consultative Group on International Agricultural Research (CGIAR) Consortium for Spatial Information (http://srtm.csi.cgiar.org/) [*Jarvis et al*., 2008]. The stream network and upstream area was determined after first filling sinks and carving sills in the 90 m DEM [*Schwanghart et al*., 2013]. We calculated several metrics to characterize topography in the Arun Valley using a combination of standard geographic information system techniques and TopoToolbox v2 [*Schwanghart and Scherler*, 2013]. Hillslope angle (degrees) and gradient (m m^{-1}) were calculated for each 90 m pixel based on its eight surrounding neighbors. Local relief was calculated for each pixel based on 1 km and 3 km radius averaging windows. Lithology was classified using the map by *Schelling* [1992]. As sampled catchments lie entirely within the LHC and HHC units (ARU-12-11 contains 3% in Tethyan sediments), we quantified catchment lithology by percent area in the High Himalayan Crystalline units (%HHC). We did not perform a more detailed analysis between units within the HHC or LHC.

3.2.1. Channel Concavity and Steepness

Channel concavity is an integral part of the stream power model for bedrock rivers [e.g., *Whipple and Tucker*, 1999; *Whipple*, 2004; *Wobus et al*., 2006] that describes channel evolution through time and varies for different rivers based on a variety of natural conditions (e.g., lithology). We calculated channel concavity for the main stem Arun and each sampled tributary by (1) standard slope-area regression [e.g., *Flint*, 1974; *Wobus et al*., 2006] and (2) least squares regression of the χ-transformed stream network [*Perron and Royden*, 2013; *Royden and Perron*, 2013]. Because orographic rainfall, as observed in the Arun Valley, has the potential to affect channel concavity in steady state river profiles [e.g., *Roe et al*., 2002], we additionally performed the slope-area and χ analysis using a TRMM rainfall-weighted flow accumulation grid. The TRMM-weighted flow accumulation grid is calculated using the routines of TopoToolbox v2 [*Schwanghart and Scherler*, 2013] and results in upstream areas that are weighted to be proportionately "larger" in regions with higher rainfall rates and proportionately "smaller" in regions with lower rainfall rates. In both cases, we separately calculated the channel concavity for the entire stream network and for the trunk stream in each catchment.

Normalized channel steepness (k_{sn}) [e.g., *Wobus et al*., 2006] was calculated for the Arun fluvial network in our study area for every 90 m pixel in the channel network. Local channel gradient was calculated for each pixel, then divided by upstream area to calculate channel steepness (k_s); we then normalize channel steepness using (1) the standard reference concavity of $\theta = 0.45$ [e.g., *Wobus et al*., 2006] and (2) the mean concavity value derived from the χ analysis of all tributaries ($\theta = 0.23 \pm 0.14$). We additionally calculated k_{sn} using a TRMM-weighted flow accumulation grid to account for the potential impact of spatially inhomogeneous rainfall, assuming that regions experiencing higher rainfall may have higher denudation rates within the basin. TRMM-weighted k_{sn} was normalized using (1) $\theta = 0.45$ and (2) $\theta = 0.20 \pm 0.14$, the mean concavity value from the TRMM-weighted χ analysis. For all channel steepness indices, catchment-mean k_{sn} was calculated for the channel network upstream of the sample location.

3.3. The ^{10}Be TCN-Derived Denudation Rates

Basin-wide denudation rates were estimated based on in situ ^{10}Be in fluvial river sands [*Brown et al*., 1995; *Bierman and Steig*, 1996; *Brown et al*., 1995; *Granger et al*., 1996]. In total, we collected and analyzed 34 samples in the Arun Valley, from the border with India in the south to the border with Tibet (China) in the north.

Our primary sample targets were (1) the main stem Arun, sampled in intervals along its N-S course; (2) tributaries to the Arun, ranging in size from $<10\,km^2$ to $>1000\,km^2$; and (3) the Sun Kosi (ARU-11-27) and Tamor (ARU-11-25) Rivers near their confluence with the Arun. Samples were taken from fresh sand banks on active channels of the main stem Arun and its tributaries. The only exception was ARU-11-12; this sample was taken from a recently abandoned or high water channel as the active channel was not accessible. In total, 7 samples were collected from the main stem Arun, one sample each from the Sun Kosi and Tamor, and 25 samples from

tributaries to the Arun. Sample site selection was also dictated by accessibility, limiting our ability to sample some major tributaries. In addition to the 34 samples collected for present-day denudation rates, we sampled paleoriver sands from a large fill terrace at Tumlingtar (ARU-12-21 and ARU-12-22) and from one smaller terrace in the lower reaches of the Arun (ARU-11-21) to quantify ^{10}Be concentrations in transiently stored sediments.

3.3.1. Sample Preparation and Processing

Samples were prepared at the University of Potsdam and the University of California–Santa Barbara following standard procedures [e.g., *Bookhagen and Strecker*, 2012]. A low-ratio ^{9}Be spike (^{10}Be/^{9}Be ratio of ~1×10^{-15}) was added to the cleaned quartz, and samples were dissolved in hydrofluoric acid. Ion-exchange chromatography was used to extract Beryllium from the dissolved samples [*von Blanckenburg et al*., 2004; *Bookhagen and Strecker*, 2012]. Samples were sent to Center for Accelerator Mass Spectrometry, Lawrence Livermore National Laboratory, USA, for accelerator mass spectrometry measurements. Ratios of ^{10}Be/^{9}Be were normalized using the 07KNSTD3110 standard (^{10}Be/^{9}Be ratio of 2.85×10^{-12}) [*Nishiizumi et al*., 2007].

3.3.2. Calculation of Catchment-Mean Denudation Rates

Production rates of cosmogenic ^{10}Be in Arun tributary catchments were calculated for every 90 m pixel of the SRTM DEM, including the effects of altitude, latitude, topography, and glaciation (see below). The same procedure was used for main stem Arun, Sun Kosi, and Tamor samples for every 1 km pixel using the U.S. Geological Survey GTOPO30 global DEM (https://lta.cr.usgs.gov/gtopo30/). Topographic shielding was calculated following *Dunne et al*. [1999]. We used the Lal/Stone scaling procedure [*Lal*, 1991; *Stone*, 2000], which takes time-dependent muogenic production and nondipole geomagnetic effects into account [*Balco et al*., 2008] and the revised ^{10}Be half-life of 1.387 ± 0.016 Myr [*Chmeleff et al*., 2010; *Korschinek et al*., 2010]. The ^{10}Be/^{9}Be concentrations were corrected using the mean of eight laboratory blanks ($1.43 \times 10^{-14} \pm 1.23 \times 10^{-15}$). The ^{10}Be concentrations were converted to erosion rates using the MATLAB functions of the CRONUS-Earth online calculator version 2.2 [*Balco et al*., 2008] in an iterative scheme provided by *Scherler et al*. [2014].

3.3.3. Ice Shielding and Glaciation

Recent studies have shown that present-day and past glaciations reduce ^{10}Be concentrations in detrital quartz and can, when unaccounted for, result in apparent denudation rates that are significantly overestimated [*Godard et al*., 2012; *Glotzbach et al*., 2013]. To mitigate this effect, we applied an ice-shielding mask to production rate calculations based on present-day glacier cover from the GLIMS glacial database; this assumes that the production rate in ice-covered areas of the catchment is zero and all ^{10}Be in the detrital sample is derived from ice-free surfaces. The ice-shielding mask was applied to three tributary catchments (ARU-11-14, ARU-11-15, and ARU-12-11) where glaciers are currently present, the main stem Arun, the Sun Kosi, and the Tamor. Currently, there is insufficient data about the glacial history of the Arun Valley available to correct for past glacial coverage [e.g., *Glotzbach et al*., 2013].

3.4. Comparison of Topographic and Climatic Metrics and Denudation Rates

To better understand regional influences on denudation rates, we performed a suite of ordinary least squares (OLS) regressions between our TCN denudation rates and catchment-mean topographic and climatic metrics. We excluded outliers (BBRS01, ARU-12-09, and ARU-12-19A), where we observe evidence of recent voluminous landsliding (see section 4.3.2), and presently glaciated tributaries. Glaciated tributaries were excluded from regression analysis because many of the topographic metrics used (e.g., k_{sn} and SSP) assume fluvial processes and are not applicable to glaciated catchments. Due to the high incidence of landsliding (see section 4.3.2) we removed ARU-11-10 and ARU-11-11 from the regression analysis. ARU-12-06 is a small tributary with a pronounced knickpoint cutting through a perched low-relief topography that may still be subjected to the impact of a previous erosion regime, and we therefore remove ARU-12-06 from the regressions.

Catchment topography has traditionally been characterized by the catchment mean or median value of a chosen metric (e.g., relief and k_{sn}). Despite this common assumption, catchment topography is often not normally distributed, especially in transient landscapes. In order to perform a more robust comparison between denudation rates and catchment climate and topography, we extend our regression analysis beyond the catchment mean or median metric value. To do this, we calculate every 5th percentile from the 10th to 90th percentile of the data and use percentile values to perform multiple OLS regressions of our catchment-mean denudation rates against catchment topographic and climatic metrics. Additionally, we performed Lilliefors [*Lilliefors*, 1967, 1969] and skewness tests to decide if catchment metrics are normally or nonnormally distributed at the 95% confidence level.

Table 1. Basin Properties for ^{10}Be TCN Sample Locations[a]

Sample ID	Sample Type	Easting (m) Universal Transverse Mercator (UTM) Z45N	Northing (m) UTM Z45N	Mean Basin Elevation (m asl)	Catchment Area (km^2)	Total Elevation Range (m)
ARU-11-01	ARUN	518661.23	3020907.28	4769.00	31260.29	8525.00
ARU-11-13	ARUN	519112.20	3043306.04	4848.00	30400.97	8236.00
ARU-11-16	ARUN	526948.20	3049019.84	4869.00	29942.76	8046.00
ARU-11-26	ARUN	515397.12	2977951.82	4544.00	33500.94	8678.00
ARU-11-28	ARUN	493136.31	2933320.99	3849.00	57979.93	8732.00
ARU-12-03	ARUN	527108.00	3049168.00	4869.00	29942.76	8048.00
ARU-12-15	ARUN	544346.00	3073168.00	4936.00	28407.20	6888.00
ARU-11-25	TAMOR	531534.41	2978676.31	2869.63	5886.36	2468.00
ARU-11-27	SUN KOSI	514554.34	2978354.97	2958.08	18100.00	3406.00
ARU-11-03	TRIBUTARY	520055.58	3022570.94	1540.16	387.60	1516.00
ARU-11-04	TRIBUTARY	517817.46	3026936.09	761.96	11.48	378.00
ARU-11-05	TRIBUTARY	515173.14	3029284.10	867.32	11.84	631.00
ARU-11-06	TRIBUTARY	513172.29	3029874.40	1606.73	74.19	1023.00
ARU-11-07	TRIBUTARY	512159.53	3032217.16	1979.48	204.45	1130.00
ARU-11-10	TRIBUTARY	514298.52	3038272.85	1173.99	2.67	384.00
ARU-11-11	TRIBUTARY	515765.77	3040048.33	1525.37	10.55	724.00
ARU-11-12	TRIBUTARY	518668.49	3043478.81	1787.03	13.20	699.00
ARU-11-14	TRIBUTARY	522720.87	3046536.67	3476.99	218.09	1328.00
ARU-11-15	TRIBUTARY	525012.39	3049015.72	4027.25	187.86	1595.00
ARU-11-18	TRIBUTARY	517935.99	3022266.40	997.13	33.25	742.00
ARU-11-20	TRIBUTARY	523924.44	3010395.96	1744.75	313.97	834.00
ARU-11-22	TRIBUTARY	526184.15	3006666.68	1177.50	35.11	817.00
ARU-11-23	TRIBUTARY	527336.27	3003012.87	1502.34	88.91	887.00
ARU-11-24	TRIBUTARY	529786.00	2999539.00	1280.30	84.19	706.00
ARU-12-01	TRIBUTARY	531001.00	3047672.00	1644.76	8.35	1431.00
ARU-12-02	TRIBUTARY	534908.00	3048053.00	2455.14	81.67	3855.00
ARU-12-06	TRIBUTARY	534070.00	3052975.00	2420.55	8.53	2128.00
ARU-12-08	TRIBUTARY	534426.00	3057465.00	2170.62	8.87	1938.00
ARU-12-09	TRIBUTARY	535079.00	3059611.00	2193.45	10.29	2248.00
ARU-12-11	TRIBUTARY	535917.00	3063263.00	4757.83	470.11	7231.00
ARU-12-12	TRIBUTARY	525213.98	3068834.00	2872.28	27.86	2584.00
ARU-12-13	TRIBUTARY	536772.00	3071756.00	3070.31	16.27	1999.00
ARU-12-19/A	TRIBUTARY	528040.00	3052286.00	2563.93	102.84	3491.00
BBRS01	TRIBUTARY	514886.16	3039168.71	1403.35	9.01	570.00

Sample ID	Mean 1 km Relief (m)	Mean 3 km Relief (m)	Mean Hillslope Angle (°)	Channel Concavity[b]	Mean k_{sn} (m$^{0.9}$)[c]	Mean k_{sn} Rainfall-Weighted (m$^{0.9}$)[d]	Mean SSP Rainfall-Weighted (W/m^2)[e]	Mean TRMM2B21 Annual Rainfall (m/yr)
ARU-11-01	416.36	841.30	15.90	0.36	235.40	366.25	63.18	0.38
ARU-11-13	412.15	832.91	15.50	0.21	411.23	441.69	57.48	0.33
ARU-11-16	408.62	825.67	15.30	0.53	318.60	512.36	53.46	0.30
ARU-11-26	416.38	842.12	16.30	0.37	156.02	203.82	69.73	0.46
ARU-11-28	559.53	1121.50	20.50	0.37	25.86	38.36	124.84	1.03
ARU-12-03	408.62	825.67	15.30	0.21	318.60	512.36	53.46	0.30
ARU-12-15	397.33	800.98	14.50	0.25	365.71	162.39	38.36	0.20
ARU-11-25	837.73	1648.68	26.38	0.42	283.63	329.67	209.50	1.65
ARU-11-27	767.19	1517.77	25.57	0.45	299.96	341.25	151.62	1.81
ARU-11-03	819.34	1718.73	25.89	0.58	191.20	300.08	212.45	2.04
ARU-11-04	526.26	945.14	18.41	0.26	87.47	109.22	163.36	1.62
ARU-11-05	634.38	1330.67	20.06	0.38	127.90	168.70	231.59	1.90
ARU-11-06	753.74	1527.71	23.90	0.27	212.53	296.88	198.39	2.18
ARU-11-07	919.51	1761.27	29.17	0.34	236.14	375.32	234.58	2.76
ARU-11-10	858.27	1637.31	25.56	0.06	163.82	211.86	404.50	1.72
ARU-11-11	885.82	1994.85	26.34	0.22	255.86	359.67	263.04	2.07
ARU-11-12	1158.52	2110.22	34.78	0.26	235.87	352.91	333.84	2.45
ARU-11-14	983.76	2037.86	29.96	0.25	325.63	428.38	329.57	2.80
ARU-11-15	1109.26	2261.01	31.67	0.25	344.25	382.11	242.46	1.67
ARU-11-18	620.36	1228.03	19.96	0.38	140.91	185.96	127.51	1.79
ARU-11-20	720.16	1412.96	22.70	0.34	223.20	275.93	127.60	1.35
ARU-11-22	706.60	1487.80	21.60	0.27	191.39	197.80	123.93	1.03
ARU-11-23	700.26	1424.97	22.17	0.20	219.21	250.31	96.07	1.23

Table 1. (continued)

Sample ID	Mean 1 km Relief (m)	Mean 3 km Relief (m)	Mean Hillslope Angle (°)	Channel Concavity[b]	Mean k_{sn} ($m^{0.9}$)[c]	Mean k_{sn} Rainfall-Weighted ($m^{0.9}$)[d]	Mean SSP Rainfall-Weighted (W/m^2)[e]	Mean TRMM2B21 Annual Rainfall (m/yr)
ARU-11-24	694.83	1377.37	24.16	0.36	191.10	215.03	108.75	1.23
ARU-12-01	691.28	1586.03	30.80	0.16	189.48	332.31	619.50	3.65
ARU-12-02	1052.03	2241.86	31.46	0.32	293.83	533.85	328.12	3.87
ARU-12-06	975.46	2214.09	26.96	0.02	285.21	545.28	365.63	4.22
ARU-12-08	968.00	2057.83	28.84	0.06	342.21	601.97	468.01	3.49
ARU-12-09	1031.90	2056.13	31.04	0.26	243.63	418.26	516.88	3.32
ARU-12-11	1010.75	2071.29	29.01	0.27	297.09	314.20	246.15	1.17
ARU-12-12	962.85	2036.90	27.93	0.16	292.02	433.36	221.28	2.66
ARU-12-13	887.10	2029.00	26.21	0.11	311.00	475.30	351.75	2.61
ARU-12-19/A	913.58	2012.41	27.40	0.31	292.67	479.49	252.16	3.30
BBRS01	808.03	1733.43	24.71	0.13	223.87	302.95	335.84	1.90

[a]Coordinates denote location of sample collection. All topographic properties derived from the 90 m CGIAR SRTM DEM [*Jarvis et al.*, 2008]. Rainfall is based on the 5 km TRMM 2B31 product [*Bookhagen and Burbank*, 2010].

[b]Values calculated using least squares regression of the chi-transformed stream network [*Perron and Royden*, 2013; *Royden and Perron*, 2013].

[c]Values calculated using standard channel concavity of $\theta = 0.45$.

[d]Values calculated using standard concavity of $\theta = 0.45$ and flow accumulation grid weighted by mean annual rainfall from TRMM (Tropical Rainfall Measurement Mission) product 2B31.

[e]Values calculated using flow accumulation grid weighted by mean annual rainfall from TRMM (Tropical Rainfall Measurement Mission) product 2B31.

3.5. The ^{10}Be Mass Balance Calculations

Standard TCN denudation rate calculation assumes that a fluvial sand sample is a uniform representative sample of the entire upstream area. Models of downstream sediment transport typically assume that particles <2 mm diameter are kept in suspension in high-energy mountain rivers [e.g., *Sklar et al.*, 2006; *Chatanantavet et al.*, 2010], further suggesting that a detrital sand sample would be uniformly sourced from the upstream area. We test this assumption by comparing ^{10}Be concentrations from main stem Arun samples from upstream regions on the border with Tibet to ^{10}Be concentrations from the confluence of the Arun, Sun Kosi, and Tamor. We performed a simple mass balance calculation to determine if the changes in ^{10}Be concentration can be achieved under the assumption of uniform upstream sediment sourcing by solving for (1) variable mass flux from the southern flanks of the Himalaya and (2) variable ^{10}Be concentration in the southern flanks of the Himalaya:

$$\mathrm{Conc._{Confluence}} = \frac{\mathrm{Area_{Tibet}MF_{Tibet}Conc._{Tibet}} + \mathrm{Area_{\mathit{H}}MF_{\mathit{H}}Conc._{\mathit{H}}}}{\mathrm{Area_{Confluence}MF_{Confluence}}} \quad (2)$$

where "Tibet" represents the area upstream of northernmost sample, "Confluence" represents the area upstream of the southernmost sample before the Sapt Kosi confluence, "H" denotes the Himalaya between the border with Tibet and the Sapt Kosi confluence, "Conc." is measured ^{10}Be concentration in the detrital sample, and MF represents the mass flux ($g\,cm^{-2}\,yr^{-1}$). To solve for mass flux, we assume that the mean ^{10}Be concentration from Arun tributaries is representative of the ^{10}Be concentration of the Himalaya in the region. To solve for variable ^{10}Be concentration, we assume that $MF_H = MF_{Confluence} - MF_{Tibet}$.

4. Results

4.1. Topography and Climate

In general, elevation and topographic steepness metrics (e.g., hillslope angle, local relief, and channel steepness) increase from south to north across the Arun Valley (Figure 3 and Table 1). Mean hillslope angle across the study area ranges from $<5°$ in the alluvial plain to $>30°$ in the Higher Himalaya (Figure 3b); 3 km radius relief similarly increases from <100 m in the alluvial plain to ~1 km in the LH, then sharply increases at the topographic transition zone into the HH, where it exceeds 2 km (Figure 3c). Discrete increases in hillslope angle and local relief are observed at both the LH and HH orographic barriers. Sampled catchments are located in the Lesser and Higher Himalaya where hillslope angle and relief are moderate to high. In sampled fluvial tributaries, mean hillslope angles range from 18° to 35°; 3 km relief ranges from 876 m to 2261 m (Figure 3 and Table 1).

Channel concavity derived from χ analysis of the main stem Arun in our study area indicates a generally graded river profile with a concavity of 0.451 until the first large knickpoint in southern Tibet (Figure 2). The channel

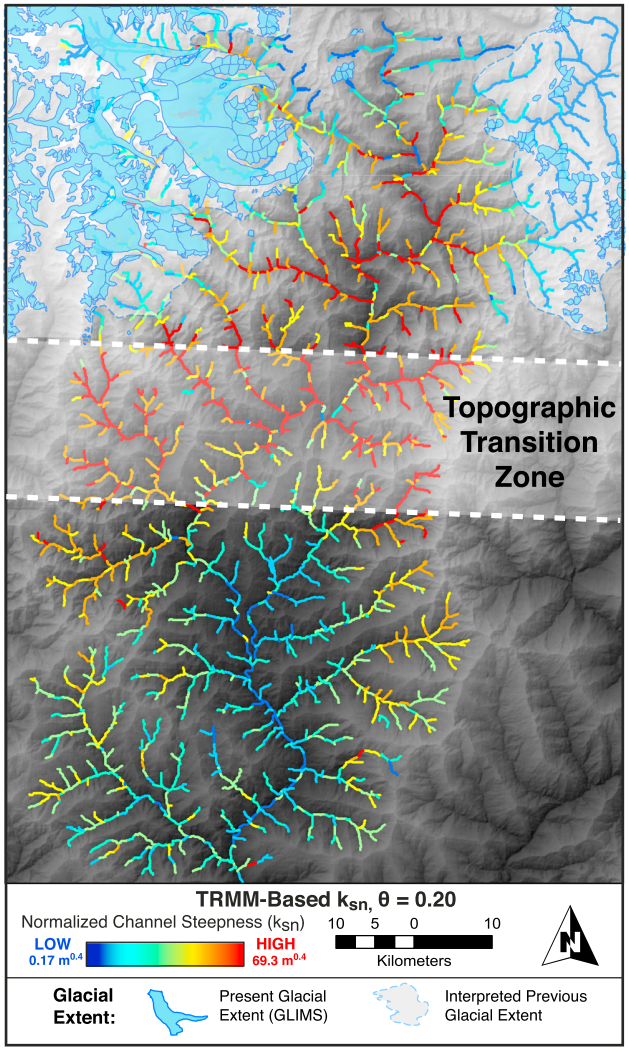

Figure 4. TRMM-weighted k_{sn} ($\theta = 0.20$). Theta values are derived from the mean tributary channel concavity values from χ analysis. Values of k_{sn} were calculated using the 90 m SRTM DEM for every pixel in the stream network, then averaged over 1 km long stream segments. All k_{sn} calculations follow a similar pattern as shown, with relatively low k_{sn} values in the LH, a steep increase in the topographic transition zone, and a continuation of high k_{sn} values in the HH. Present-day glacial extent based on the GLIMS Glacier Database and the authors' interpretation of previous glacial extent is shown in blue. Normalized channel steepness values are low in these regions corresponding to glacial valley morphology.

concavity of tributary streams decreases steadily from 0.57 in the south to 0.02 in the north (Table 1 and Figure 3f), indicating more uniformly steep channels approaching Tibet; tributary channel concavity calculated from TRMM-weighted flow accumulation does not significantly differ from the nonweighted concavity values at the 95% confidence level. Unlike hillslope angle and relief, no discrete break in concavity values is observed at the topographic transition zone.

Normalized channel steepness is low throughout the Lesser Himalaya in the main stem Arun and tributary channels but increases rapidly at the topographic transition zone (Figure 4). Throughout the Higher Himalaya, k_{sn} remains high; low values in the upper reaches of some tributaries correspond to glacial valley morphology. Catchment-mean values of k_{sn} for fully fluvial sample tributaries range from 87 m$^{0.9}$ to 342 m$^{0.9}$, normalized by $\theta = 0.45$; for $\theta = 0.23$ catchment-mean k_{sn} values range from 2.78 m$^{0.46}$ to 11.34 m$^{0.46}$ (Table 1). Minimum and maximum k_{sn} values correspond to small tributaries ($<$20 km^2) that lie entirely in the LHC and HHC units, respectively. TRMM-weighted flow accumulation results in higher k_{sn} values throughout the HH and LH, ranging from 109 m$^{0.9}$ to 602 m$^{0.9}$ normalized by $\theta = 0.45$ and 1.92 m$^{0.4}$ to 9.17 m$^{0.4}$ normalized by $\theta = 0.20$ (see Table S1 in the supporting information). TRMM-weighted k_{sn} has a strong, positive linear correlation with unweighted k_{sn} ($R^2 = 0.88$, 0.97 for standard reference concavity ($\theta = 0.45$) and χ-determined channel concavity, respectively).

Mean annual rainfall follows a steep, two-tiered gradient (cf. section 2.1), increasing from ~2 m yr^{-1} in the alluvial plain to $>$3 m yr^{-1} at the front of the LH/Siwaliks, then decreases rapidly to $<$2 m yr^{-1} in the rain shadow of the LH orographic barrier; rainfall steadily increases over the next 40 km approaching the HH orographic barrier to a peak of ~4 m yr^{-1}, then decreases into Tibet (Figure 3d). Within our sampled catchments, catchment-mean annual rainfall ranges from 1.03 m yr^{-1} (ARU-11-22) directly north of the LH orographic barrier to 4.22 m yr^{-1} in the Higher Himalaya (ARU-12-06).

TRMM-weighted SSP follows a similar pattern to mean annual precipitation (Figure 3e), with peaks of ~500 W m^{-2} at the LH and HH orographic barriers and variably high values (200–500 W m^{-2}) throughout the HH. A sixfold range of catchment-mean SSP values is observed in sampled tributaries, with catchment-mean SSP ranging from 104 W m^{-2} in the Lesser Himalaya to 620 W m^{-2} (Table 1) at the topographic transition zone, where rainfall and channel slopes are high.

Table 2. The ^{10}Be TCN Results[a]

	Sample ID	Quartz Mass (g)[b]	Muonic Production Rate (atoms/(g yr))[c]	Mean Spalliogenic Production Rate (atoms/(g yr))[c]	Topographic Shielding[d]	Ice Shielding[e]	^{10}Be Conc. (atoms/g)[f]	±^{10}Be (atoms/g)	Basin-Averaged Denudation (mm/yr)[g]	Apparent Age (Year)[h]	Used in Regression Analysis?
Arun, Sun Kosi, Tamor	ARU-11-01	149.37	0.74	65.16	0.999	0.943	1.78E + 05	3.18E + 03	0.22 ± 0.02	2.74E + 03	NO[i]
	ARU-11-13	72.41	0.75	67.12	0.999	0.941	1.95E74E + 05	3.34E + 03	0.21 ± 0.02	2.92E + 03	NO[i]
	ARU-11-16	69.87	0.76	67.89	0.999	0.940	1.71E + 05	2.88E + 03	0.24 ± 0.02	2.53E + 03	NO[i]
	ARU-11-25	124.71	0.48	26.39	0.997	0.849	1.18E + 04	4.44E + 02	1.39 ± 0.11	445.4164	NO[i]
	ARU-11-26	125.70	0.71	62.83	0.999	0.946	4.84E + 04	9.88E + 02	0.75 ± 0.06	7.79E + 02	NO[i]
	ARU-11-27	88.55	0.50	30.34	0.997	0.930	2.29E + 04	5.17E + 02	0.82 ± 0.06	745.5625	NO[i]
	ARU-11-28	153.06	0.62	48.59	0.998	0.938	3.13E + 04	8.22E + 02	0.91 ± 0.07	6.48E + 02	NO[i]
	ARU-12-03	102.78	0.76	67.65	0.999	0.940	2.85E + 04	6.97E + 02	1.35 ± 0.11	4.22E + 02	NO[i]
	ARU-12-15	152.31	0.77	69.32	0.999	0.943	1.41E + 05	2.73E + 03	0.29 ± 0.02	2.04E + 03	NO[i]
Lesser Himalaya	ARU-11-03	170.66	0.31	12.55	0.964	1.000	1.94E + 04	2.60E + 02	0.47 ± 0.03	1.50E + 03	YES
	ARU-11-04	108.20	0.24	6.46	0.993	1.000	2.99E + 04	7.18E + 02	0.19 ± 0.01	4.48E + 03	YES
	ARU-11-05	173.45	0.24	6.97	0.987	1.000	2.67E + 04	4.17E + 02	0.22 ± 0.01	3.72E + 03	YES
	ARU-11-06	216.55	0.31	12.44	0.983	1.000	2.10E + 04	6.16E + 02	0.43 ± 0.03	1.66E + 03	YES
	ARU-11-07	99.87	0.35	15.77	0.970	1.000	5.75E + 04	1.03E + 03	0.19 ± 0.01	3.60E + 03	YES
	ARU-11-18	96.92	0.26	7.76	0.984	1.000	3.66E + 04	5.08E + 02	0.18 ± 0.01	4.59E + 03	YES
	ARU-11-20	46.62	0.33	13.54	0.985	1.000	1.80E + 04	1.49E + 02	0.54 ± 0.04	1.31E + 03	YES
	ARU-11-22	85.74	0.27	8.89	0.981	1.000	1.66E + 04	1.56E + 02	0.42 ± 0.03	1.82E + 03	YES
	ARU-11-23	138.93	0.30	11.56	0.935	1.000	4.88E + 04	8.43E + 02	0.18 ± 0.01	4.15E + 03	YES
	ARU-11-24	226.03	0.28	9.60	0.982	1.000	3.88E + 04	7.64E + 02	0.19 ± 0.01	3.95E + 03	YES
Topographic Transition Zone	ARU-11-10	122.01	0.27	8.67	0.938	1.000	5.61E + 03	7.27E + 01	1.21 ± 0.08	6.32E + 02	NO[j]
	ARU-11-11	110.40	0.30	11.17	0.971	1.000	8.24E + 03	5.67E + 01	1.00 ± 0.06	7.24E + 02	NO[j]
	ARU-11-12	103.54	0.33	13.13	0.835	1.000	1.21E + 04	3.58E + 02	0.78 ± 0.06	9.05E + 02	YES
	ARU-12-01	202.79	0.31	11.99	0.981	1.000	1.71E + 04	5.74E + 02	0.51 ± 0.04	1.40E + 03	YES
	ARU-12-02	200.02	0.40	20.79	0.958	1.000	2.59E + 04	3.81E + 02	0.53 ± 0.04	1.24E + 03	YES
	ARU-12-06	206.34	0.39	19.68	0.974	1.000	9.12E + 04	1.59E + 03	0.15 ± 0.01	4.59E + 03	NO[l]
	BBRS01	104.18	0.2861	9.94	0.980	1.000	1.61E + 03	2.50E + 01	4.58 ± 0.30	1.58E + 02	NO[j]
Higher Himalaya	ARU-11-14 l	107.16	0.55	37.45	0.921	0.944	1.65E + 04	2.09E + 02	1.36 ± 0.10	4.39E + 02	NO[k]
	ARU-11-15 l	163.54	0.64	31.30	0.925	0.710	2.07E + 04	2.83E + 02	0.94 ± 0.07	6.57E + 02	NO[k]
	ARU-12-08	166.05	0.37	16.83	0.960	1.000	7.85E + 03	2.99E + 01	1.44 ± 0.10	4.61E + 02	YES
	ARU-12-09	149.74	0.37	17.19	0.955	1.000	4.97E + 03	2.95E + 02	2.30 ± 0.21	2.86E + 02	NO[j]
	ARU-12-11	142.05	0.75	36.29	0.951	0.688	1.48E + 04	2.92E + 02	1.48 ± 0.11	4.05E + 02	NO[k]
	ARU-12-12	215.14	0.45	27.26	0.865	1.000	2.47E + 04	1.30E + 03	0.68 ± 0.06	9.32E + 02	YES
	ARU-12-13	190.31	0.47	28.99	0.725	1.000	3.87E + 04	1.18E + 03	0.47 ± 0.04	1.33E + 03	YES
	ARU-12-19A l	138.89	0.4164	22.43	0.971	1.000	1.36E + 03	2.72E + 01	10.36 ± 0.76	6.01E + 01	NO[j]

[a]The ^{10}Be/^{9}Be ratios were measured at the Lawrence Livermore National Laboratory and were normalized using the 07KNSTD3110 standard [*Nishiizumi et al.*, 2007]. Denudation rates are calculated with a bedrock density of 2.6 g cm^{-3} and an attenuation length of $\lambda = 160$ g cm^{2}. Shielding values of 1 denote no topographic or ice shielding.

[b]Mass of quartz dissolved for ^{10}Be extraction.

[c]Production rate calculations were performed for every grid point of the 90 m DEM using the Lal/Stone scaling scheme [*Lal*, 1991; *Stone*, 2000]. Production rate depends on altitude, latitude, and topographic and ice shielding.

[d]Topographic shielding based on 90 m SRTM DEM following *Dunne et al.* [1999].

[e]Ice shielding is based on present ice coverage from the National Snow and Ice Data Center (NSIDC) Global Land Ice Measurements from Space (GLIMS) database.

[f]Derived from blank-corrected AMS measurements undertaken at Lawrence Livermore National Laboratory and normalized to Integrated Computing Network standard [*Nishiizumi et al.*, 2007].

[g]Denudation rates are calculated with a bedrock density of 2.6 g cm^{-3} and an attenuation length for spallation of $\lambda = 160$ g cm^{2}.

[h]Time over which denudation rates are averaged (year).

[i]Main stem sample or other tributary that integrates entire topographic and climatic gradient.

[j]Landslide-impacted tributary with apparent denudation rate that likely does not represent temporal average.

[k]Glaciated tributary.

[l]Small tributary (<10 km^{2}) with pronounced transient profile.

[m]Catchment lies within multiple physiographic regions but has been grouped with dominant area.

AGU Journal of Geophysical Research: Earth Surface

10.1002/2014JF003410

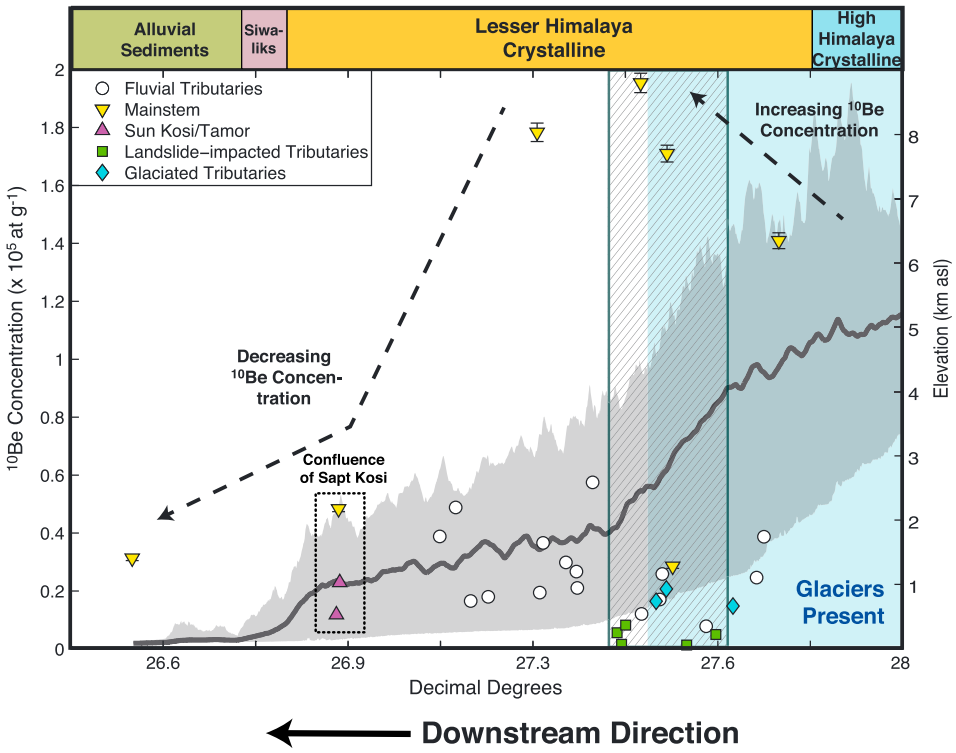

Figure 5. The ^{10}Be concentration from main stem Arun (yellow triangle), Sun Kosi and Tamor Rivers (purple triangle), fluvial tributaries (white circle), glaciated tributaries (blue diamond), and landslide-impacted tributaries (green square). Lithology along the Arun River from *Grujic et al.* [2011]. Mean elevation is shown in black with minimum/maximum elevation in shaded gray, taken from a 75 km swath along the Arun Valley. Glaciated regions of the Higher Himalaya are shaded blue. A region of marked landsliding is shown as gray hatch. Note the increasing ^{10}Be concentration south of the Tibetan Plateau through the HHC and the decreasing ^{10}Be concentration in the LH, which we associated with downstream fining of material derived from the Tibetan Plateau.

4.2. The ^{10}Be Concentration in River-Sediment Samples

Sample ^{10}Be concentrations are recorded in Table 2 and Figure 5. We observe two main signals in main stem Arun ^{10}Be concentration: (1) a high ^{10}Be concentration in the north of the study area and (2) a low ^{10}Be concentration in the lower reaches of the Arun and Sapt Kosi. Downstream ^{10}Be concentrations in the main stem Arun are similar to ^{10}Be concentrations from tributaries in the Higher and Lesser Himalaya, as well as low ^{10}Be concentrations observed from the Sun Kosi and Tamor Rivers. Tributary ^{10}Be concentrations are an order of magnitude lower than the northern, high ^{10}Be main stem Arun samples and show a northward decrease from the LH to HH. Within the tributaries, the lowest ^{10}Be concentrations are observed within the transition to the Higher Himalaya and in presently glaciated catchments.

4.3. The ^{10}Be Catchment-Mean Denudation Rates

4.3.1. Main Stem Arun, Sun Kosi, Tamor, and Sapt Kosi

Catchment-mean denudation rates in the main stem Arun decrease from the confluence of the Arun, Tamor, and Sun Kosi Rivers (0.75 ± 0.06 mm yr^{-1} at ARU-11-26) northward to the border with Tibet (0.24 ± 0.02 mm yr^{-1}; $n = 4$) (Figure 6a and Table 2). Near their confluence with the Arun, the Sun Kosi and Tamor have denudation rates of 0.82 ± 0.06 mm yr^{-1} and 1.39 ± 0.11 mm yr^{-1}, respectively. The Sapt Kosi, measured in the alluvial plain, records a denudation rate of 0.91 ± 0.07 mm yr^{-1}. This marks a fivefold decrease in main stem denudation rates across the Arun/Sapt Kosi River from the alluvial plain to Tibet. Similarly, the relatively high denudation rates in the Sun Kosi and Tamor Rivers that drain the southern flanks of the Himalaya are 5 to 7 times greater than in the upper reaches of the Arun.

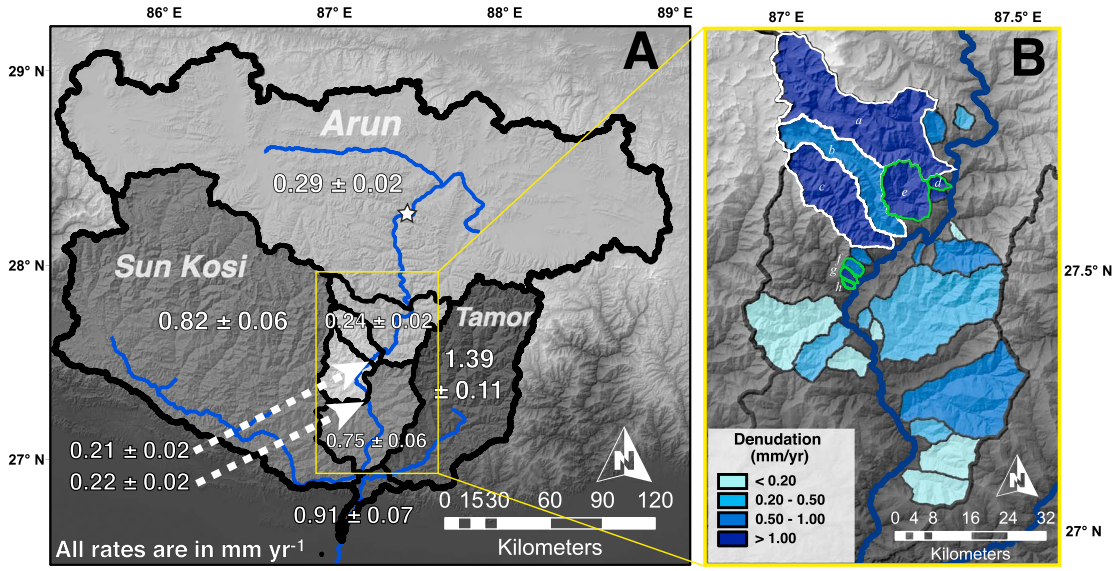

Figure 6. TCN catchment-mean denudation rates for (a) the main stem Arun, Sun Kosi, Tamor, and Sapt Kosi, showing northward decrease in apparent denudation rate, and (b) sampled tributaries to the Arun, showing northward increase in the Himalaya. Denudation rates are shown alongside the river network (blue), elevation (hillshade), and the major knickzones in the main stem Arun (star). All denudation rates are shown in mm yr^{-1}. Glaciated tributaries are outlined in white ((a) ARU-12-11, (b) ARU-11-15, and (c) ARU-11-14). Landslide-impacted tributaries outlined in green ((d) ARU-12-09, (e) ARU-12-19A, (f) ARU-11-11, (g) BBRS01, and (h) ARU-11-10).

4.3.2. Tributary Catchments

The highly dynamic orogenic environment of the Himalaya includes several nonfluvial processes (e.g., landsliding and glaciation) that complicate the interpretation of TCN-derived denudation rates [e.g., *Brown et al.*, 1995; *Niemi et al.*, 2005; *Yanites et al.*, 2009; *Godard et al.*, 2012]. To avoid these complications, we first present denudation rates from fluvial tributaries that do not show evidence of recent landsliding or glaciation, then describe results from glacial and landslide-impacted catchments. Fluvial tributaries show an order-of-magnitude northward increase in catchment-mean denudation rates from the Lesser to Higher Himalaya (Figure 6b and Table 2). Denudation rates in the LH are low to moderate (<0.5 mm yr^{-1}) and vary over a relatively narrow range (~0.2–0.5 mm yr^{-1}) ($n=10$). Denudation rates increase in the topographic transition zone (~0.5–0.8 mm yr^{-1}) ($n=3$) and are highest in the Higher Himalaya (1.44 mm yr^{-1} in ARU-12-08), then appear to decrease further into the orogen (e.g., 0.47 mm yr^{-1} in ARU-12-13) ($n=3$). Higher denudation rates in the topographic transition zone and the Higher Himalaya, however, may be mainly driven by glacial and hillslope processes.

Glaciers occupy some tributary valleys in the Higher Himalaya (Figure 6) and have the potential to alter TCN denudation rates. We observe high denudation rates in the heavily glaciated Barun Valley (ARU-12-11, 1.48 ± 0.11 mm yr^{-1}), as well as in two less glaciated valleys directly south of the Barun (ARU-11-14, 1.36 ± 0.10 mm yr^{-1}; ARU-11-15, 0.94 ± 0.07 mm yr^{-1}). However, there are fundamental problems interpreting denudation rates from these valleys: (1) shielding of bedrock from cosmogenic rays by glacial ice, (2) the assumption of steady state erosion through time [*Bierman and Steig*, 1996], and (3) the assumption that each area in the basin contributes sediment in proportion to long-term erosion rates. The dynamics of glacial erosion and sediment delivery are complicated and poorly understood and are likely not steady through time. All of these processes may result in an overestimation of true denudation rates [*Godard et al.*, 2012; *Glotzbach et al.*, 2013]. The application of an ice-shielding grid to the denudation rate calculation accounts for glacial shielding of sediment in the detrital sample, thus producing more reliable denudation rate estimates. However, we note that we cannot account for possible nonsteady state or proportionate denudation through time and therefore consider denudation rates from glacial catchments as apparent denudation rates that may differ from temporal averages.

Landsliding is common throughout the steep-slope terrain of the Himalaya [e.g., *Bookhagen et al.*, 2005a; *Dahal and Hasegawa*, 2008]. Because landslides frequently erode material from below the absorption depth of cosmogenic nuclides, they have the potential to dilute the ^{10}Be signal within a detrital sample. If the catchment is sufficiently large and well-mixed, TCN concentrations from landslide-dominated catchments can still

provide reliable denudation rates [*Niemi et al.*, 2005; *Yanites et al.*, 2009]. However, small, poorly mixed catchments or samples collected shortly after recent landslide events may result in calculated denudation rates that do not reflect the time-averaged denudation rate [*Yanites et al.*, 2009]. To quantify the potential impact of landsliding on our samples, we mapped visible landslide scars in all sampled tributary catchments using high-resolution imagery from Google Earth (see data repository Figure S1 in the supporting information for further information) [*Fisher et al.*, 2012]. While small landslides are ubiquitous in the study area, we observed five catchments with a pronounced amount of landsliding as a percentage of total catchment area: three small catchments ($<10\,km^2$) in the topographic transition zone (ARU-11-10, ARU-11-11, and BBRS01) and one small catchment ($\sim10\,km^2$) and one medium-sized catchment ($\sim100\,km^2$) in the Higher Himalaya (ARU-12-09 and ARU-12-19A, respectively). In each catchment, the landslide area is markedly higher than the 0.001% of total catchment area proposed by *Yanites et al.* [2009] that will still produce a reliable denudation rate. BBRS01, ARU-12-09, and ARU-12-19A have anomalously high apparent denudation rates (4–10 mm yr^{-1}), and the five landslide-affected tributaries represent the lowest observed ^{10}Be concentrations in our study area. Due to the likely recent delivery of material from below the ^{10}Be absorption depth from landslides in these samples, measured ^{10}Be concentrations may not be representative of the temporal average. We therefore consider the calculated denudation rates as maximum apparent denudation rates.

A more complex picture of denudation across the Arun Valley emerges when we consider the entire set of denudation rates, incorporating glacial and landslide-impacted apparent denudation rates. We observe largely fluvial denudation through the Lesser Himalaya, with low to moderate rates that do not vary considerably (0.2–0.5 mm yr^{-1}). In the topographic transition zone, fluvial denudation rates increase (0.5–0.8 mm yr^{-1}) concurrent with an increase in landsliding, with apparent denudation rates of ~5 mm yr^{-1}. This marks the changeover to an erosion regime that is more variable in both rates and processes. Significant landsliding continues at the front of the Higher Himalaya (ARU-12-09 and ARU-12-19A) with maximum denudation rates in excess of 10 mm yr^{-1}. Glaciation additionally begins to play a role in the Higher Himalaya, maintaining denudation rates similar to the highest fluvial denudation rates (~0.9–1.5 mm yr^{-1}). Fluvial denudation rates, meanwhile, appear to decrease into the Higher Himalaya away from the high-relief, high-rainfall frontal zone (e.g., ARU-12-13).

5. Discussion

The ^{10}Be TCN samples from the Arun Valley record a pronounced northward increase in denudation rates across the Himalaya in tributary catchments and a fourfold decrease in main stem denudation rates from the lower reaches of the Arun to the upper reaches bordering Tibet. In a dynamic environment such as the Himalaya, several factors can influence ^{10}Be concentrations (e.g., nonuniform sediment sourcing and transient sediment storage) [*Bierman and Steig*, 1996; *Granger et al.*, 1996; *von Blanckenburg*, 2005]. However, we did not find evidence of major impacts from potentially variable sediment sourcing or transiently stored sediments on our measured ^{10}Be concentrations and calculated denudation rates (see Text S1 in the supporting information for details of the analyses performed). Below, we further discuss the interpretation of ^{10}Be concentrations and denudation rate calculation.

5.1. Downstream Evolution of Main Stem ^{10}Be Concentration

In order to better understand the impact of regional factors on denudation rates, we first consider measured ^{10}Be concentrations directly (Table 2 and Figure 5). For the following discussion, we interpret the two distinct groupings of ^{10}Be concentrations discussed in section 4.2 as (1) the Tibetan signal, comprising high ^{10}Be concentrations measured in the upper reaches of the main stem Arun, and (2) the Himalayan signal, comprising low ^{10}Be concentrations measured in tributaries to the Arun, the Sun Kosi, and Tamor and from the downstream sections of the main stem Arun.

5.1.1. Downstream Fining

One of the most prominent features of the ^{10}Be concentrations is the pronounced downstream reduction of ^{10}Be in the main stem Arun (Figure 5). This order-of-magnitude difference must be the result of either (1) a large sediment flux from the Himalaya able to sufficiently dilute the ^{10}Be signal from Tibet to the levels recorded at the Sapt Kosi confluence or (2) significant sediment storage within the Himalayan section of the valley. Comparing the ^{10}Be concentration in ARU-11-13 (high ^{10}Be) and ARU-11-26 (low ^{10}Be), we solve the mass balance problem presented in equation (2) as

$$\mathrm{Conc.}_{\mathrm{ARU-11-26}} = \frac{\mathrm{Area}_{\mathrm{ARU-11-13}}\mathrm{MF}_{\mathrm{ARU-11-13}}\mathrm{Conc.}_{\mathrm{ARU-11-13}} + \mathrm{Area}_{H}\mathrm{MF}_{H}\mathrm{Conc.}_{H}}{\mathrm{Area}_{\mathrm{ARU-11-26}}\mathrm{MF}_{\mathrm{ARU-11-26}}} \quad (3)$$

where H denotes the Himalaya between Tibet and the Sapt Kosi confluence and MF represents the mass flux ($\mathrm{g\,cm^{-2}\,yr^{-1}}$) (Tables 1 and 2 and Figure 7). To solve for mass flux, we assume that the mean ^{10}Be concentration from Arun tributaries ($2.56 \times 10^4 \pm 4.6 \times 10^2$ at $\mathrm{g^{-1}}$; $n = 20$) is representative of the ^{10}Be concentration of the entire Himalayan section of the valley. However, using this ^{10}Be concentration, the resulting mass flux for the southern flanks of the Himalaya is negative ($-0.12\,\mathrm{g\,cm^{-2}\,yr^{-1}}$), indicating sediment storage in a region where no significant modern sediment storage is observed (see Text S1). As such, it is impossible to reconcile the ^{10}Be concentration measured at ARU-11-26 with a positive mass flux from the Himalaya under these assumptions. Similarly, if we define the Himalayan mass flux as $\mathrm{MF}_H = \mathrm{MF}_{26} - \mathrm{MF}_{13}$ ($0.15\,\mathrm{g\,cm^{-2}\,yr^{-1}}$), the calculated ^{10}Be concentration is likewise negative, a physical impossibility unless the system is undergoing either sedimentation or sediment loss through grain fining. We therefore assume that the collected sample cannot be a uniform representation of the upstream area. Instead, we suggest that downstream sediment fining continues for particles <2 mm, resulting in the Tibetan sediment passing through our 250–750 μm sample sieve. This effect is identifiable in the Arun due to the large difference in ^{10}Be production rate between the high-altitude, low-relief Tibetan region (high ^{10}Be production) and the relatively low-altitude, high-relief Himalaya (low ^{10}Be production; Figure 7). However, similar problems could remain undetected in sufficiently large watersheds with uniform or near-uniform ^{10}Be production rates, such as the Sun Kosi or Tamor or large watersheds in other orogens.

The exclusion of upstream sediment grains from the analyzed samples results in estimated denudation rates that do not reflect the entire upstream area. We therefore interpret the calculated "high" denudation rates from the main stem Arun (e.g., ARU-11-26, $0.75\,\mathrm{mm\,yr^{-1}}$) as primarily reflecting the denudation rate of the southern flanks of the Himalaya and not the Tibetan section of the watershed, resulting in an overestimation of the true denudation rate for the watershed. This finding calls into question the use of large watersheds or distal sampling sites to characterize regional denudation rates, particularly in the Himalaya and in trans-Himalayan rivers. Recent studies have highlighted differences in ^{10}Be concentrations in different grain size fractions from detrital sand samples [*McPhillips et al.*, 2014; *Puchol et al.*, 2014]. While the motivation for these analyses has been primarily to quantify the impact of landslide processes and focus on larger grain and cobble sizes, measuring ^{10}Be concentration from various grain size fractions, including those <200 μm, may also mitigate the problems downstream fining poses for denudation rate estimation.

5.1.2. Climate-Driven Dilution of ^{10}Be Concentration

The northernmost main stem sample, ARU-12-15, has a noticeably lower ^{10}Be concentration than nearby samples from the northern main stem Arun, resulting in a local southward increase in ^{10}Be concentration before the more drastic decrease near the topographic transition zone. This southward increase of ^{10}Be is restricted to the glaciated portion of the Higher Himalaya (Figure 5). Glaciated catchments measure among the lowest ^{10}Be concentrations in the Arun Valley. North of our study area, extensive glaciation exists on the northern flank of the HH. Specifically, a large and heavily glaciated tributary that drains the northern slopes of the Sagarmatha/Everest massif joins the Arun approximately 10 km north of the sampling point of ARU-12-15. This nearby influx of highly shielded sediment may locally dilute the ^{10}Be concentration measured at ARU-12-15 before it is measured again over 40 km downstream. A modeled ^{10}Be concentration for ARU-12-15 assuming an erosion rate of $0.2\,\mathrm{mm\,yr^{-1}}$ (approximate denudation rate from nearby main stem samples ARU-11-01, ARU-11-13, and ARU-11-16; Figure 6 and Table 2) and the mean upstream production rate is nearly 1.5 times the measured value (2.09×10^5 at $\mathrm{g^{-1}}$ modeled as opposed to 1.41×10^5 at $\mathrm{g^{-1}}$ measured in ARU-12-15), suggesting that a large, local influx of low ^{10}Be sediment is responsible for the ^{10}Be concentration measured at ARU-12-15. We also observe a relatively low ^{10}Be concentration (and therefore higher apparent denudation rate) in the Tamor compared to the main stem Arun or the Sun Kosi. Glaciers occupy a larger area of the Tamor Basin (~15%) compared to these other large rivers (~5–7%), and the higher degree of glaciation in the Tamor may be the cause of lower ^{10}Be concentrations and higher apparent denudation rates.

In addition to local dilution from glacial input, we observe one main stem sample in the northern section of the study area (ARU-12-03) with a low ^{10}Be ratio where we would expect to measure a high ^{10}Be signal from Tibet. This sample was taken less than 2 km downstream of a medium-sized tributary with large, recent landslides

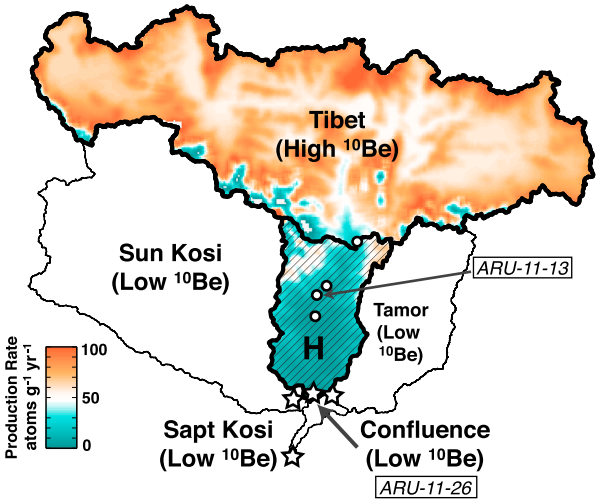

Figure 7. Schematic of main stem ^{10}Be concentration mass balance calculations on map showing ^{10}Be production rates. Observed ^{10}Be concentrations at main stem Arun and other major river sand sample locations are shown as circles (high observed ^{10}Be, ~10^5 atoms g^{-1}) or stars (low observed ^{10}Be, ~10^4 atoms g^{-1}). The Tibet, Himalaya (H), and confluence locations used in the mass balance calculation are highlighted; Himalayan section of the catchment shown in hatch. Higher ^{10}Be production rates (atoms/(g yr) in Tibet compared to the Himalaya results in a distinct signal that allows for the detection of downstream fining from Tibet to the confluence of the Sapt Kosi.

(ARU-12-19A) that are likely to have diluted the ^{10}Be concentration of the main stem sample (ARU-12-19A has the lowest measured ^{10}Be concentration in our data set). Landsliding predates the 2012 field season when samples ARU-12-03 and ARU-12-19A were collected. The timing of the large landslides in ARU-12-19A is not easily constrained with high-resolution imagery due to high cloud cover and poor image resolution, but some landslide scars are visible as early as 2009. A nearby sample collected in 2011 (ARU-11-16) does not show the low ^{10}Be concentration derived from the landslide. This may be due to the timing of the landslides or to different sediment sourcing in the river system during and after the monsoon season [e.g., *Lupker et al.*, 2012].

It is notable that landslide-impacted tributaries are focused at the front of the Higher Himalaya where elevation, rainfall, and relief rapidly increase from the Lesser Himalaya. While relief and elevation remain high throughout the Higher Himalaya, rainfall decreases northward toward the high topography. Landslide-impacted tributaries are focused in a zone where both relief and rainfall peak, showing the importance of focused rainfall in triggering mass movements (Figure 5).

5.2. Denudation Gradient Across the Arun Valley

In general, denudation rates in tributaries to the Arun increase from south to north coincident with the increase of topographic metrics such as hillslope angle, k_{sn}, and local relief (Figure 3 and Table 3). Due to the tectonic window, nearly all sampled basins are composed of both LHC and HHC units and no major lithologic boundaries are crossed by the main stem Arun in our study area (Figure 1d). Although the percentage of HHC rocks increases northward as the Arun Tectonic Window narrows and denudation rates increase, no relationship is observed between catchment-mean denudation rates and lithology (see Figure S2).

The across-strike pattern of northward increasing denudation rates we observe is similar to those reported by *Godard et al.* [2014] and *Scherler et al.* [2014]. In both studies, denudation rates in the Lesser Himalaya are reported between ~0.1 and 0.5 mm yr^{-1} and increase rapidly at the transition to the Higher Himalaya, where denudation rates exceed 1 mm yr^{-1}. The similar pattern between the Arun Valley and the results of studies where denudation rates are fit to tectonic drivers suggests that, at first order, a similar process drives the rates and pattern of denudation in the Arun Valley. We note, however, that the highest rates of denudation (>2 mm yr^{-1}) reported by *Godard et al.* [2014] and *Scherler et al.* [2014] are derived from regions with high rainfall rates and high local relief, similar to where we found the highest incidence of landslide-impacted catchments in the Arun, and may be overestimations of true denudation rate.

Previous studies have suggested a nonlinear relationship between topographic metrics (e.g., slope and k_{sn}) and denudation rates, such that for a given topographic metric, [*topographic metric*]^b~*denudation rate*, with power law values ranging from $b = 1$ to $b = 4$ [*Safran et al.*, 2005; *Ouimet et al.*, 2009; *DiBiase et al.*, 2010; *DiBiase and Whipple*, 2011; *Bookhagen and Strecker*, 2012; *Fisher et al.*, 2013; *Scherler et al.*, 2014]. We observe the highest correlation between denudation rate and χ-determined k_{sn} ($R^2 = 0.66$ for area-weighted k_{sn}, $R^2 = 0.67$ for TRMM-weighted k_{sn}, compared to $R^2 = 0.54$, 0.57 for area- and TRMM-weighted for the standard k_{sn} normalized by $\theta = 0.45$). The power law relationship between k_{sn} and denudation rate in our data set ranges from

Table 3. Results of the Regression Analysis Between ^{10}Be TCN-Derived Denudation Rates and Catchment Climate and Topographic Metrics[a]

	All Fluvial Tributaries					Excluding Landslide-Affected Tributaries				
	R^2	*F* value	*P* value	*a*	*b*	R^2	*F* Value	*P* Value	*a*	*b*
Metric	$y = ax^b$					$y = ax^b$				
Topographic metrics										
Hillslope gradient	0.19	5.80	0.0277	1.32E + 00	1.35E + 00	0.35	13.01	0.0029	1.49E + 00	1.67E + 00
1 km relief	0.23	6.48	0.0209	1.47E − 05	1.57E + 00	0.37	11.81	0.0040	2.35E − 06	1.84E + 00
Area SSP	0.26	2.81	0.1121	3.56E − 02	5.10E − 01	0.26	2.98	0.1062	3.56E − 02	5.10E − 01
Area k_{sn} ($\theta = 0.45$)	0.18	3.79	0.0682	1.26E − 03	1.11E + 00	0.54	11.33	0.0046	1.08E − 05	1.96E + 00
Area k_{sn} ($\theta = 0.23$)	0.26	5.47	0.0318	5.72E − 02	1.14E + 00	0.66	16.59	0.0011	1.14E − 02	1.90E + 00
Climatic metrics										
TRMM	0.04	1.19	0.2910	3.73E − 01	3.43E − 01	0.23	6.40	0.0241	1.90E − 01	9.22E − 01
TRMM SSP	0.35	4.99	0.0392	1.06E − 02	6.93E − 01	0.35	7.10	0.0185	1.06E − 02	6.93E − 01
TRMM k_{sn} ($\theta = 0.45$)	0.15	3.30	0.0872	1.26E − 02	6.44E − 01	0.57	14.83	0.0018	2.04E − 04	1.33E + 00
TRMM k_{sn} ($\theta = 0.20$)	0.23	5.04	0.0384	1.30E − 01	8.52E − 01	0.67	19.14	0.0006	3.44E − 02	1.59E + 00

[a] All regression coefficients were calculated using an ordinary least squares (OLS) power law regression model.

$b = 1.33 - 1.96$, similar to studies in other active tectonic environments (Figure 8, and references therein). Fluvial incision models [e.g., *Whipple and Tucker*, 1999; *Snyder et al.*, 2003; *Sklar and Dietrich*, 2004; *Lague et al.*, 2005] predict a monotonic relationship between channel slope and rock uplift at steady state, and numerous studies have shown positive correlations between k_{sn} and rock uplift [e.g., *Snyder et al.*, 2000; *Kirby and Whipple*, 2001; *DiBiase et al.*, 2010]. The large knickpoints in the main stem Arun upstream of our study area (Figure 2) and several perched low-relief surfaces (see section 5.3 below), however, cast doubt on the assumption that the Arun is in landscape equilibrium. Localized high k_{sn} values have also been shown to correlate with areas where the river is adjusting to a transient perturbation. When this is the case, high k_{sn} values will follow knickzones as they propagate through the channel network as it adjusts to the perturbation (e.g., base-level drop and change in uplift rates) [e.g., *Wobus et al.*, 2006]. Such a perturbation can be climatic or tectonic; however, several studies along strike have found evidence for relatively high uplift rates in the Higher Himalaya with respect to the Lesser Himalaya [e.g., *Lavé and Avouac*, 2001; *Godard et al.*, 2004; *Herman et al.*, 2010; *Coutand et al.*, 2014]. We therefore associate high k_{sn} and corresponding high denudation rates with locally high uplift rates.

Although we observe a moderately strong correlation between denudation rates and k_{sn}, our denudation rates correlate poorly with many other standard topographic and climatic metrics (Table 3). We were not able to constrain several factors of the fluvial network, such as channel width, depth, and geometry. Recent studies have highlighted the importance of channel width and geometry in the stream power model and in erosional proxies, such as specific stream power [*Fisher et al.*, 2013]. In our SSP calculations, we scaled channel width to discharge following a power law relationship [*Knighton*, 1999; *Whipple*, 2004; *Craddock et al.*, 2007]. This approach results in channel width increasing nonlinearly as upstream area increases. However, the low concavity values we derived from χ analysis of the fluvial network indicate that many channels in the Arun continue to have steep channels gradients in their lower reaches and thus narrow channel widths [*Yanites et al.*, 2010; *Fisher et al.*, 2012]. Discharge scaling is therefore likely an inaccurate estimate of channel width in this environment and may explain why SSP poorly describes denudation rates in the Arun compared to other orogens [e.g., *Bookhagen*

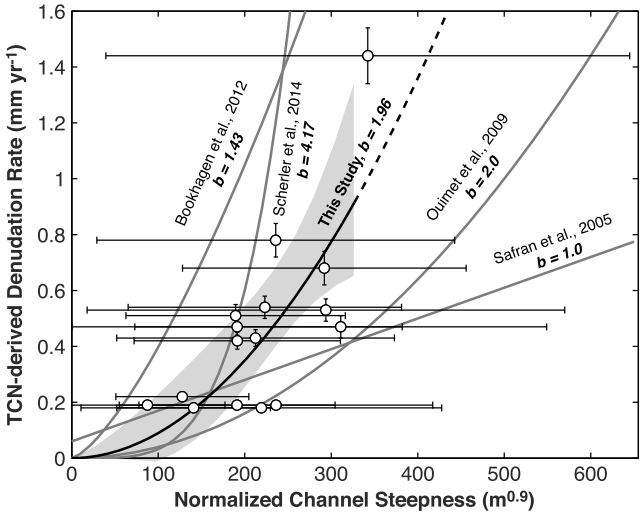

Figure 8. Power law relationship of the standard area-weighted k_{sn} ($\theta = 0.45$, $R^2 = 0.54$) and denudation rates, shown with 95% confidence interval in shaded gray compared to published relationships from *Bookhagen and Strecker* [2012], *Ouimet et al.* [2009], *Safran et al.* [2005], and *Scherler et al.* [2014]. The observed power law exponent b (from the relationship $y = ax^b$) for the Arun is $b = 1.96$ (95% confidence interval; upper and lower bounds $b = 0.33$, 1.19).

and Strecker, 2012]. Similar scaling issues may exist in other regions with steep channels and low concavity.

5.3. Percentile Regression of Catchment Characteristics and Denudation Rates

In dynamic landscapes, topography and topographic metrics within a catchment may not always follow a normal or Gaussian distribution. Such skewed or multimodal catchment distributions can result in mean or median values that are not the best representatives of the data population. Lilliefors tests suggested a nonnormal distribution of elevation, hillslope gradient, 1 km local relief, and mean annual rainfall in all sampled catchments at a 95% confidence level. On the other hand, k_{sn} values do not show evidence of nonnormal distributions in some basins; however, this result may be an artifact of sample size, as a smaller sample is less likely to reject the null hypothesis of normal distribution. Similarly, we found a systematic positive skew (right-tail) in the distribution of hillslope gradient and k_{sn} (see Table S2).

Figure 9 shows an example of how such nonnormal distributions may arise within a catchment as the result of transient topography. Relatively small areas of perched, low-relief topography were observed throughout the study area. Here a low-relief area in the upper reaches of the catchment (Figure 9c) results in a bimodal

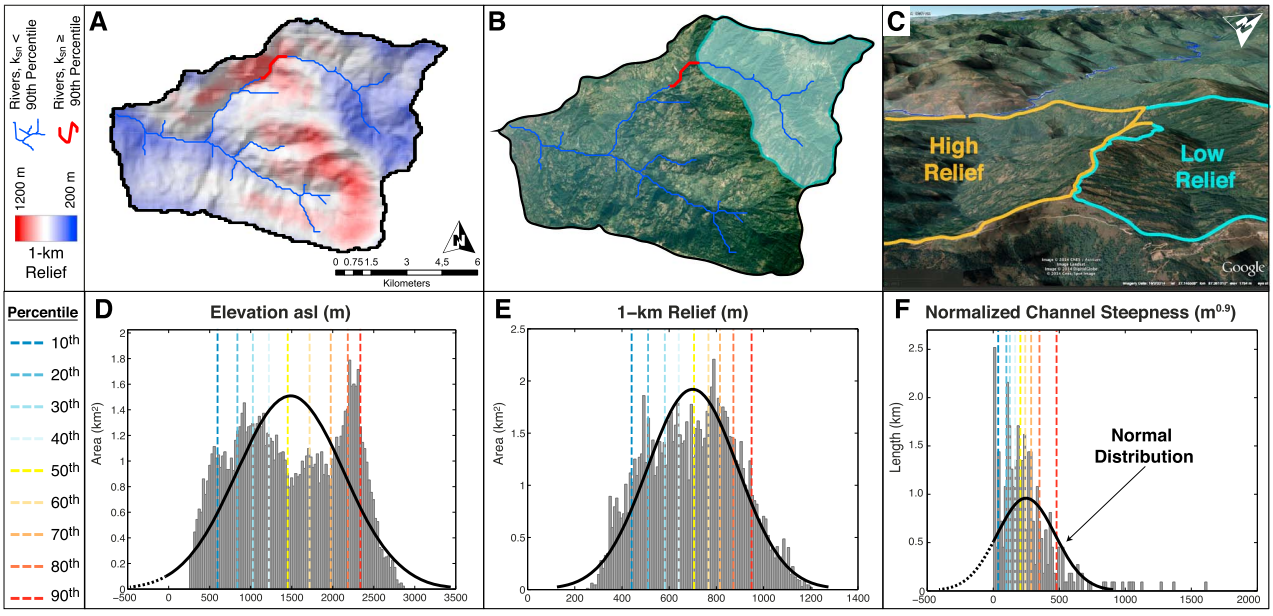

Figure 9. Example catchment demonstrating nonnormal topographic distribution (ARU-11-23). (a) The 1 km relief map of the catchment, paired with 90th percentile of k_{sn} located at the foot of the transient surface. (b) Our interpretation of the relief map, with perched, low-relief surface shown in blue. (c) Google Earth view of low-relief topography. Histograms of topographic metrics: (d) elevation (m asl), (e) 1 km relief (m), and (f) k_{sn} ($m^{0.46}$), shown with approximate normal distribution (black line) and percentile values (dashed lines).

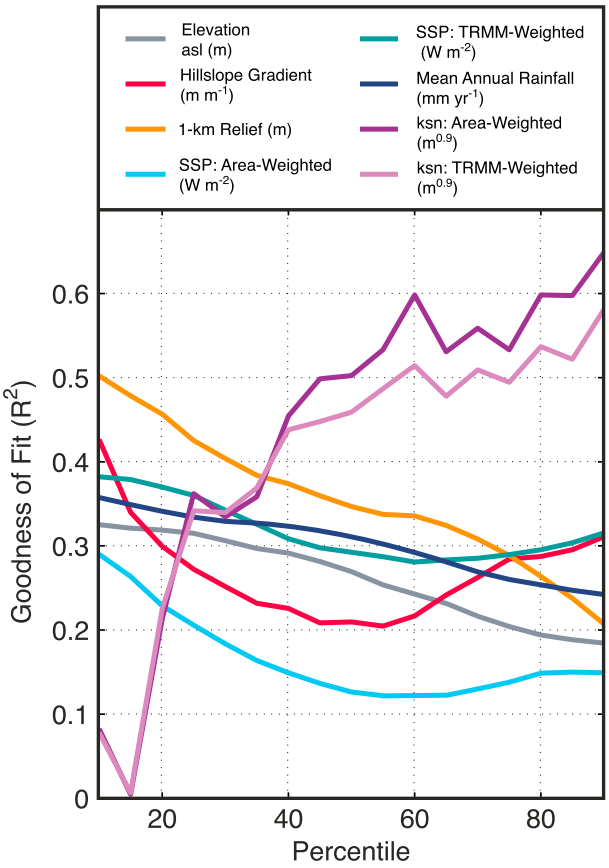

Figure 10. Regression results between various catchment-mean topographic and climatic metrics and denudation rates based on percentiles of catchment metrics and denudation rates, showing the variable goodness of fit depending on which catchment value is used. Normalized channel steepness values calculated using channel concavity from χ analysis, showing the moderately strong correlation between k_{sn} and denudation rates.

distribution of elevation and quasi-bimodal distribution of 1 km local relief (Figures 9d and 9e). High k_{sn} is focused at the foot of the perched low-relief area where knickpoints propagate into relict topographies and the catchment moves toward equilibrium. As shown in the histograms of elevation, local relief, and k_{sn}, the normal distribution and associated statistics (mean and standard deviation) assumed by averaging do not fit the data population. While catchments with transient features are likely to be the most problematic in this regard, evidence for skewed and nonnormal distributions were found in all catchments for nearly all metrics.

Figure 10 shows the goodness of fit (R^2) of the regression analysis using the catchment-mean value and the catchment percentile values of various topographic and climatic metrics. The strength of the correlation between denudation rate and catchment topography and climate varies by as much as a factor of 6 (e.g., k_{sn}) depending on the metric and the percentile used. In the case of k_{sn}, the correlation increases positively with the percentile used. However, the systematic positive skew in the distribution of k_{sn} values in sampled catchments suggests that channel segments where $k_{sn} >$ 90th percentile comprise relatively small portion of the channel network. Thus, the rate of denudation may be most sensitive to, and focused at, locations in the catchment that do not correspond with standard averaging techniques (e.g., mean, median, or mode). The disconnect between catchment average statistics, the catchment distribution of topographic metrics, and the areas (sometimes small) that correlate best with denudation rates highlights the problem of uniformly characterizing catchments in a highly dynamic landscape. While such topographic metrics are useful first-order approximations, they are far from exact proxies for the processes that drive erosion.

6. Conclusions

Based on our 34 new ^{10}Be TCN measurements in eastern Nepal combined with field observations and topographic and climatic analyses, we reach the following conclusions:

1. Catchment-mean denudation rates show an order-of-magnitude northward increase from the Lesser Himalaya to the Higher Himalaya, as elevation, hillslope, and channel steepness increase. The spatial pattern of denudation rates is most strongly correlated with normalized channel steepness, following a nonlinear power law relationship $[k_{sn}]^b$~*denudation rate* with best fit parameter for $b = 1.89$ ($\theta = 0.23$, $R^2 = 0.66$, 95% confidence interval $b_{lower} = 1.01$, $b_{upper} = 2.27$). The strong relationship between denudation rates and k_{sn}, as well as a similar observed pattern of denudation rates derived from studies arguing for tectonic drivers [*Godard et al.*, 2014; *Scherler et al.*, 2014], suggests a prominent role of rock uplift in forcing denudation rates in the Himalaya [cf. *Godard et al.*, 2014; *Scherler et al.*, 2014]. However, we observe

multiple climatic influences on the processes of erosion in the Arun Valley, such as the extent of glaciation and localized landsliding in the area of peak rainfall and relief.

2. Nonfluvial processes such as extensive glaciation and landsliding upstream of sample sites can cause local dilution of ^{10}Be concentrations in detrital samples. Local dilution of detrital sand from the main stem Arun demonstrates that such processes can even impact very large watersheds that are typically assumed to integrate upstream perturbations (e.g., landslides). When left unaccounted for, dilution of ^{10}Be concentration caused by local geomorphic processes could result in overestimation of catchment-mean denudation rates.
3. Downstream fining of fluvial sand continues past $<$2 mm diameter grains, resulting in sand grains sourced from upstream (Tibetan) sections of the watershed passing through the 250 μm sieve in samples collected downstream. Therefore, downstream main stem Arun samples are likely representative of the Himalayan section of the catchment, rather than the entire watershed. Although the Arun provides a well-suited setting to record this effect, the exclusion of fined upstream sediment may also occur undetected in large watersheds in other mountain belts. We therefore call into question the use of distal detrital samples to characterize denudation rates in extensive mountainous catchments. Consequently, sampling multiple grain sizes in high-mountain environments may yield a more robust characterization of denudation rates, including potentially fined upstream sediments.
4. Nonnormal distribution of catchment topographic and climatic parameters in many sampled basins in our study highlights the importance of using caution when choosing how to characterize catchments with regard to erosion processes. Skewed and multimodal distributions of catchment topography and variations in sensitivity to denudation rates suggest that while such topographic metrics may be a useful first-order approximation of the processes that drive erosion at the regional scale, they are far from ideal proxies at the catchment scale.

Acknowledgments

Data supporting Figure 10 are available in Table S3. This project was funded by the graduate school GRK1364 "Shaping Earth's Surface in a Variable Environment: Interactions between tectonics, climate, and biosphere in the African-Asian monsoonal region" of the German Science Foundation (Deutsche Forschungsgemeinschaft (DFG) project GRK 1364/2). In addition, funding for one field season and all analytical work was provided by the HIMPAC research project (Himalayas: Modern and Past Climates), funded by DFG (STR 373/27-1 and 28-1) We thank Dirk Scherler and Taylor Schildgen for their valuable discussions; Ed Sobel, Burch Fisher, and Jessica Thompson for their help with laboratory work; and Bhim Chand of Earth's Paradise GeoTrekking for logistical support in the field. Finally, we thank Nicole Gasparini, Elizabeth Safran, and Ken Ferrier for their constructive input into greatly improving this manuscript.

References

Avouac, J. P. (2003), Mountain building, erosion, and the seismic cycle in the Nepal Himalaya, *Adv. Geophys.*, *46*, 1–80.

Balco, G., J. O. Stone, N. A. Lifton, and T. J. Dunai (2008), A complete and easily accessible means of calculating surface exposure ages or erosion rates from ^{10}Be and ^{26}Al measurements, *Quat. Geochronol.*, *3*(3), 174–195.

Bierman, P., and E. J. Steig (1996), Estimating rates of denudation using cosmogenic isotope abundances in sediment, *Earth Surf. Processes Landforms*, *21*, 125–139.

Bookhagen, B., and D. W. Burbank (2006), Topography, relief, and TRMM-derived rainfall variations along the Himalaya, *Geophys. Res. Lett.*, *33*, L08405, doi:10.1029/2006GL026037.

Bookhagen, B., and D. W. Burbank (2010), Toward a complete Himalayan hydrological budget: Spatiotemporal distribution of snowmelt and rainfall and their impact on river discharge, *J. Geophys. Res.*, *115*, F03019, doi:10.1029/2009JF001426.

Bookhagen, B., and M. R. Strecker (2012), Spatiotemporal trends in erosion rates across a pronounced rainfall gradient: Examples from the southern central Andes, *Earth Planet. Sci. Lett.*, *327–328*, 97–110.

Bookhagen, B., R. C. Thiede, and M. R. Strecker (2005a), Abnormal monsoon years and their control on erosion and sediment flux in the high, arid northwest Himalaya, *Earth Planet. Sci. Lett.*, *231*(1–2), 131–146.

Bookhagen, B., R. C. Thiede, and M. R. Strecker (2005b), Late Quaternary intensified monsoon phases control landscape evolution in the northwest Himalaya, *Geology*, *33*(2), 149–152.

Bray, H. E., and S. Stokes (2004), Temporal patterns of arid-humid transitions in the south-eastern Arabian Peninsula based on optical dating, *Geomorphology*, *59*(1–4), 271–280.

Brown, E. T., R. F. Stallard, M. C. Larsen, G. M. Raisbeck, and F. Yiou (1995), Denudation rates determined from the accumulation of in situ-produced ^{10}Be in the Luquillo Experimental Forest, Puerto Rico, *Earth Planet. Sci. Lett.*, *129*(1–4), 193–202.

Büdel, J. (1982), *Climatic Geomorphology*, 444 pp., Princeton Univ. Press, Princeton, N. J.

Burbank, D. W., A. E. Blythe, J. Putkonen, B. Pratt-Sitaula, E. Gabet, M. Oskin, A. Barros, and T. P. Ojha (2003), Decoupling of erosion and precipitation in the Himalayas, *Nature*, *426*(6967), 652–655.

Carpenter, C., and R. Zomer (1996), Forest ecology of the Makalu-Barun National Park and Conservation Area, Nepal, *Mt. Res. Dev.*, *16*(2), 135–148.

Charney, J. G. (1969), The Intertropical Convergence Zone and the Hadley circulation of the atmosphere, Proc. WMO/IUCG Symp. Nu- mer. Weather Predict. Jpn. Meteorol. Agency, Ill, 73-79.

Chatanantavet, P., E. Lajeunesse, G. Parker, L. Malverti, and P. Meunier (2010), Physically based model of downstream fining in bedrock streams with lateral input, *Water Resour. Res.*, *46*, W02518, doi:10.1029/2008WR007208.

Chmeleff, J., F. von Blanckenburg, K. Kossert, and D. Jakob (2010), Determination of the ^{10}Be half-life by multicollector ICP-MS and liquid scintillation counting, *Nucl. Instrum. Methods Phys. Res., Sect. B*, *268*(2), 192–199.

Clift, P. D., N. Shimizu, G. D. Layne, J. S. Blusztajn, C. Gaedicke, H.-U. Schlüer, M. K. Clark, and S. Amjad (2001), Development of the Indus Fan and its significance for the erosional history of the Western Himalaya and Karakoram, *Geol. Soc. Am. Bull.*, *113*(8), 1039–1051.

Coutand, I., D. M. Whipp, D. Grujic, M. Bernet, M. G. Fellin, B. Bookhagen, K. R. Landry, S. K. Ghalley, and C. Duncan (2014), Geometry and kinematics of the Main Himalayan Thrust and Neogene crustal exhumation in the Bhutanese Himalaya derived from inversion of multithermochronologic data, *J. Geophys. Res. Solid Earth*, *119*, 1446–1481, doi:10.1002/2013JB010891.

Craddock, W. H., D. W. Burbank, B. Bookhagen, and E. J. Gabet (2007), Bedrock channel geometry along an orographic rainfall gradient in the upper Marsyandi River valley in central Nepal, *J. Geophys. Res.*, *112*, F03007, doi:10.1029/2006JF000589.

Curray, J. R., F. J. Emmel, and D. G. Moore (2002), The Bengal Fan: Morphology, geometry, stratigraphy, history and processes, *Mar. Pet. Geol.*, *19*(10), 1191–1223.

Dahal, R. K., and S. Hasegawa (2008), Representative rainfall thresholds for landslides in the Nepal Himalaya, *Geomorphology*, *100*(3–4), 429–443.
DiBiase, R. A., and K. X. Whipple (2011), The influence of erosion thresholds and runoff variability on the relationships among topography, climate, and erosion rate, *J. Geophys. Res.*, *116*, F04036, doi:10.1029/2011JF002095.
DiBiase, R. A., K. X. Whipple, A. M. Heimsath, and W. B. Ouimet (2010), Landscape form and millennial erosion rates in the San Gabriel Mountains, CA, *Earth Planet. Sci. Lett.*, *289*(1–2), 134–144.
Dunne, J., D. Elmore, and P. Muzikar (1999), Scaling factors for the rates of production of cosmogenic nuclides for geometric shielding and attenuation at depth on sloped surfaces, *Geomorphology*, *27*(1–2), 3–11.
Ferrier, K. L., K. L. Huppert, and J. T. Perron (2013a), Climatic control of bedrock river incision, *Nature*, *496*(7444), 206–209.
Ferrier, K. L., J. T. Perron, S. Mukhopadhyay, M. Rosener, J. D. Stock, K. L. Huppert, and M. Slosberg (2013b), Covariation of climate and long-term erosion rates across a steep rainfall gradient on the Hawaiian island of Kaua'i, *Geol. Soc. Am. Bull.*, *125*(7/8), 1146–1163, doi:10.1130/B30726.1.
Fisher, G. B., C. B. Amos, B. Bookhagen, D. W. Burbank, and V. Godard (2012), Channel widths, landslides, faults, and beyond: The new world order of high-spatial resolution Google Earth imagery in the study of Earth surface processes, *Geol. Soc. Am. Spec. Pap.*, *492*, 1–22.
Fisher, G. B., B. Bookhagen, and C. B. Amos (2013), Channel planform geometry and slopes from freely available high-spatial resolution imagery and DEM fusion: Implications for channel width scalings, erosion proxies, and fluvial signatures in tectonically active landscapes, *Geomorphology*, *194*, 46–56.
Fleitmann, D., S. J. Burns, M. Mudelsee, U. Neff, J. Kramers, A. Mangini, and A. Matter (2003), Holocene forcing of the Indian monsoon recorded in a stalagmite from Southern Oman, *Science*, *300*(5626), 1737–1739.
Flint, J. J. (1974), Stream gradient as a function of order, magnitude, and discharge, *Water Resour. Res.*, *10*, 969–973, doi:10.1029/WR010i005p00969.
Gadgil, S. (2003), The Indian monsoon and its variability, *Annu. Rev. Earth Planet. Sci.*, *31*(1), 429–467.
GLIMS, and National Snow and Ice Data Center (2005), Updated 2012, GLIMS Glacier Database, National Snow and Ice Data Center, Boulder, Colorado USA, doi:10.7265/N5V98602.
Glotzbach, C., M. Röttjer, A. Hampel, R. Hetzel, and P. W. Kubik (2013), Quantifying the impact of former glaciation on catchment-wide denudation rates derived from cosmogenic ^{10}Be, *Terra Nova*, *26*(3), 186–194.
Godard, V., R. Cattin, and J. Lavé (2004), Numerical modeling of mountain building: Interplay between erosion law and crustal rheology, *Geophys. Res. Lett.*, *31*, L23607, doi:10.1029/2004GL021006.
Godard, V., D. W. Burbank, D. L. Bourlès, B. Bookhagen, R. Braucher, and G. B. Fisher (2012), Impact of glacial erosion on ^{10}Be concentrations in fluvial sediments of the Marsyandi catchment, central Nepal, *J. Geophys. Res.*, *117*, F03013, doi:10.1029/2011JF002230.
Godard, V., D. L. Bourlés, F. Spinabella, D. W. Burbank, B. Bookhagen, G. B. Fisher, A. Moulin, and L. Léanni (2014), Dominance of tectonics over climate in Himalayan denudation, *Geology*, *42*(3), 243–246.
Goodbred, S. L., and S. A. Kuehl (2000), Enormous Ganges-Brahmaputra sediment discharge during strengthened early Holocene monsoon, *Geology*, *28*(12), 1083–1086.
Granger, D. E., J. W. Kirchner, and R. Finkel (1996), Spatially averaged long-term erosion rates measured from in situ-produced cosmogenic nuclides in alluvial sediment, *J. Geol.*, *104*(3), 249–257.
Granger, D. E., N. A. Lifton, and J. K. Willenbring (2013), A cosmic trip: 25 years of cosmogenic nuclides in geology, *Geol. Soc. Am. Bull.*, *125*(9–10), 1379–1402.
Grujic, D., C. J. Warren, and J. L. Wooden (2011), Rapid synconvergent exhumation of Miocene-aged lower orogenic crust in the eastern Himalaya, *Lithosphere*, *3*(5), 346–366.
Hales, T. C., and J. J. Roering (2005), Climate-controlled variations in scree production, Southern Alps, New Zealand, *Geology*, *33*(9), 701–704.
Herman, F., et al. (2010), Exhumation, crustal deformation, and thermal structure of the Nepal Himalaya derived from the inversion of thermochronological and thermobarometric data and modeling of the topography, *J. Geophys. Res.*, *115*, B06407, doi:10.1029/2008JB006126.
Herman, F., D. Seward, P. G. Valla, A. Carter, B. Kohn, S. D. Willett, and T. A. Ehlers (2013), Worldwide acceleration of mountain erosion under a cooling climate, *Nature*, *504*(7480), 423–426.
Hirschmiller, J., D. Grujic, B. Bookhagen, I. Coutand, P. Huyghe, J.-L. Mugnier, and T. Ojha (2014), What controls the growth of the Himalayan foreland fold-and-thrust belt?, *Geology*, *42*, 247–250.
Hodges, K. V., J. Hurtado, and K. X. Whipple (2001), Southward extrusion of Tibetan crust and its effect on Himalayan tectonics, *Tectonics*, *20*(6), 799–809, doi:10.1029/2001TC001281.
Hodges, K. V., C. Wobus, K. Ruhl, T. Schildgen, and K. Whipple (2004), Quaternary deformation, river steepening, and heavy precipitation at the front of the Higher Himalayan ranges, *Earth Planet. Sci. Lett.*, *220*(3–4), 379–389.
Huntington, K. W., A. E. Blythe, and K. V. Hodges (2006), Climate change and late Pliocene acceleration of erosion in the Himalaya, *Earth Planet. Sci. Lett.*, *252*(1–2), 107–118.
Jarvis, A., H. I. Reuter, A. Nelson, and E. Guevara (2008), Hole-filled SRTM for the globe version 4. available from the CGIAR-CSI SRTM 90m Database. [Available at http://srtm.csi.cgiar.org.]
Kirby, E., and K. Whipple (2001), Quantifying differential rock-uplift rates via stream profile analysis, *Geology*, *29*(5), 415–418.
Knighton, A. D. (1999), Downstream variation in stream power, *Geomorphology*, *29*(3–4), 293–306.
Korschinek, G., et al. (2010), A new value for the half-life of ^{10}Be by Heavy-Ion Elastic Recoil Detection and liquid scintillation counting, *Nucl. Instrum. Methods Phys. Res., Sect. B*, *268*(2), 187–191.
Lague, D. (2014), The stream power river incision model: Evidence, theory and beyond, *Earth Surf. Processes Landforms*, *39*(1), 38–61.
Lague, D., N. Hovius, and P. Davy (2005), Discharge, discharge variability, and the bedrock channel profile, *J. Geophys. Res.*, *110*, F04006, doi:10.1029/2004JF000259.
Lal, D. (1991), Cosmic ray labeling of erosion surfaces: In situ nuclide production rates and erosion models, *Earth Planet. Sci. Lett.*, *104*(2–4), 424–439.
Lavé, J., and J. P. Avouac (2001), Fluvial incision and tectonic uplift across the Himalayas of central Nepal, *J. Geophys. Res.*, *106*(B11), 26,561–26,591, doi:10.1029/2001JB000359.
Lilliefors, H. W. (1967), On the Kolmogorov-Smirnov test for normality with mean and variance unknown, *J. Am. Stat. Assoc.*, *62*, 399–402.
Lilliefors, H. W. (1969), On the Kolmogorov-Smirnov test for the exponential distribution with mean unknown, *J. Am. Stat. Assoc.*, *64*, 387–389.
Lupker, M., P.-H. Blard, J. Lavé, C. France-Lanord, L. Leanni, N. Puchol, J. Charreau, and D. Bourlès (2012), ^{10}Be-derived Himalayan denudation rates and sediment budgets in the Ganga basin, *Earth Planet. Sci. Lett.*, *333–334*, 146–156.
McPhillips, D., P. R. Bierman, and D. H. Rood (2014), Millennial-scale record of landslides in the Andes consistent with earthquake trigger, *Nat. Geosci.*, *7*(12), 925–930.

Meier, K., and E. Hiltner (1993), Deformation and metamorphism within the Main Central Thrust zone, Arun Tectonic Window, eastern Nepal, in *Himalayan Tectonics*, edited by P. J. Treloar and M. P. Searle, *Geol. Soc. London Spec. Publ.*, 74, 511–523.
Milliman, J. D., and J. D. M. Syvitski (1992), Geomorphic/tectonic control of sediment discharge to the ocean: The importance of small mountainous rivers, *J. Geol.*, *100*, 525–544.
Molnar, P., and P. England (1990), Late Cenozoic uplift of mountain ranges and global climate change: Chicken or egg?, *Nature*, *346*(6279), 29–34.
Molnar, P., and P. Tapponnier (1975), Cenozoic tectonics of Asia: Effects of a continental collision: Features of recent continental tectonics in Asia can be interpreted as results of the India-Eurasia collision, *Science*, *189*(4201), 419–426.
Montgomery, D. R., and D. B. Stolar (2006), Reconsidering Himalayan river anticlines, *Geomorphology*, *82*(1–2), 4–15.
Moon, S., C. Page Chamberlain, K. Blisniuk, N. Levine, D. H. Rood, and G. E. Hilley (2011), Climatic control of denudation in the deglaciated landscape of the Washington Cascades, *Nat. Geosci.*, *4*(7), 469–473.
Niemi, N. A., M. Oskin, D. W. Burbank, A. M. Heimsath, and E. J. Gabet (2005), Effects of bedrock landslides on cosmogenically determined erosion rates, *Earth Planet. Sci. Lett.*, *237*(3–4), 480–498.
Nishiizumi, K., M. Imamura, M. W. Caffee, J. R. Southon, R. C. Finkel, and J. McAninch (2007), Absolute calibration of ^{10}Be AMS standards, *Nucl. Instrum. Methods Phys. Res., Sect. B*, *258*(2), 403–413.
Ouimet, W. B., K. X. Whipple, and D. E. Granger (2009), Beyond threshold hillslopes: Channel adjustment to base-level fall in tectonically active mountain ranges, *Geology*, *37*(7), 579–582.
Perron, J. T., and L. Royden (2013), An integral approach to bedrock river profile analysis, *Earth Surf. Processes Landforms*, *38*, 570–576.
Prins, M. A., and G. Postma (2000), Effects of climate, sea level, and tectonics unraveled for last deglaciation turbidite records of the Arabian Sea, *Geology*, *28*(4), 375–378.
Puchol, N., J. Lavé, M. Lupker, P.-H. Blard, F. Gallo, and C. France-Lanord (2014), Grain-size dependent concentration of cosmogenic ^{10}Be and erosion dynamics in a landslide-dominated Himalayan watershed, *Geomorphology*, *224*, 55–68.
Reiners, P. W., T. A. Ehlers, S. G. Mitchell, and D. R. Montgomery (2003), Coupled spatial variations in precipitation and long-term erosion rates across the Washington Cascades, *Nature*, *426*(6967), 645–647.
Riebe, C. S., J. W. Kirchner, D. E. Granger, and R. C. Finkel (2001), Strong tectonic and weak climatic control of long-term chemical weathering rates, *Geology*, *29*(6), 511–514.
Riebe, C. S., J. W. Kirchner, and R. C. Finkel (2004), Erosional and climatic effects on long-term chemical weathering rates in granitic landscapes spanning diverse climate regimes, *Earth Planet. Sci. Lett.*, *224*(3–4), 547–562.
Roe, G. H., D. R. Montgomery, and B. Hallet (2002), Effects of orographic precipitation variations on the concavity of steady-state river profiles, *Geology*, *30*(2), 143–146.
Roe, G. H., K. X. Whipple, and J. K. Fletcher (2008), Feedbacks among climate, erosion, and tectonics in a critical wedge orogen, *Am. J. Sci.*, *308*(7), 815–842.
Royden, L., and J. T. Perron (2013), Solutions of the stream power equation and application to the evolution of river longitudinal profiles, *J. Geophys. Res. Earth Surf.*, *118*, 497–518, doi:10.1002/jgrf.20031.
Safran, E. B., P. R. Bierman, R. Aalto, T. Dunne, K. X. Whipple, and M. Caffee (2005), Erosion rates driven by channel network incision in the Bolivian Andes, *Earth Surf. Processes Landforms*, *30*(8), 1007–1024.
Schelling, D. (1992), The tectonostratigraphy and structure of the eastern Nepal Himalaya, *Tectonics*, *11*(5), 925–943, doi:10.1029/92TC00213.
Scherler, D., B. Bookhagen, and M. R. Strecker (2014), Tectonic control on ^{10}Be-derived erosion rates in the Garhwal Himalaya, India, *J. Geophys. Res. Earth Surf.*, *119*, 83–105, doi:10.1002/2013JF002955.
Schwanghart, W., and D. Scherler (2013), Short communication: TopoToolbox 2: An efficient and user-friendly tool for Earth surface sciences, *Earth Surf. Dyn. Discuss.*, *1*(1), 261–275.
Schwanghart, W., G. Groom, N. J. Kuhn, and G. Heckrath (2013), Flow network derivation from a high resolution DEM in a low relief, agrarian landscape, *Earth Surf. Processes Landforms*, *38*(13), 1576–1586.
Seeber, L., and V. Gornitz (1983), River profiles along the Himalayan arc as indicators of active tectonics, *Tectonophysics*, *92*, 355–467.
Sklar, L. S., and W. E. Dietrich (2004), A mechanistic model for river incision into bedrock by saltating bed load, *Water Resour. Res.*, *40*, W06301, doi:10.1029/2003WR002496.
Sklar, L. S., W. E. Dietrich, E. Foufoula-Georgiou, B. Lashermes, and D. Bellugi (2006), Do gravel bed river size distributions record channel network structure?, *Water Resour. Res.*, *42*, W06D18, doi:10.1029/2006WR005035.
Snyder, N. P., K. X. Whipple, G. E. Tucker, and D. J. Merritts (2000), Landscape response to tectonic forcing: Digital elevation model analysis of stream profiles in the Mendocino Triple Junction region, Northern California, *Geol. Soc. Am. Bull.*, *112*(8), 1250–1263.
Snyder, N. P., K. X. Whipple, G. E. Tucker, and D. J. Merritts (2003), Channel response to tectonic forcing: Field analysis of stream morphology and hydrology in the Mendocino Triple Junction region, Northern California, *Geomorphology*, *53*(1–2), 97–127.
Stone, J. O. (2000), Air pressure and cosmogenic isotope production, *J. Geophys. Res.*, *105*(B10), 23,753–723,759, doi:10.1029/2000JB900181.
Thamban, M., V. Purnachandra Rao, and R. R. Schneider (2002), Reconstruction of late Quaternary monsoon oscillations based on clay mineral proxies using sediment cores from the western margin of India, *Mar. Geol.*, *186*(3–4), 527–539.
Thiede, R. C., J. R. N. Arrowsmith, B. Bookhagen, M. O. McWilliams, E. R. Sobel, and M. R. Strecker (2005), From tectonically to erosionally controlled development of the Himalayan orogen, *Geology*, *33*(8), 689–692.
von Blanckenburg, F. (2005), The control mechanisms of erosion and weathering at basin scale from cosmogenic nuclides in river sediment, *Earth Planet. Sci. Lett.*, *237*(3–4), 462–479.
von Blanckenburg, F., T. Hewawasam, and P. W. Kubik (2004), Cosmogenic nuclide evidence for low weathering and denudation in the wet, tropical highlands of Sri Lanka, *J. Geophys. Res.*, *109*, F03008, doi:10.1029/2003JF000049.
Wager, L. R. (1937), The Arun River drainage pattern and the rise of the Himalaya, *Geogr. J.*, *89*(3), 239–250.
Whipple, K. X. (2004), Bedrock rivers and the geomorphology of active orogens, *Annu. Rev. Earth Planet Sci.*, *32*, 151–185.
Whipple, K. X., and G. E. Tucker (1999), Dynamics of the stream-power river incision model: Implications for height limits of mountain ranges, landscape response timescales, and research needs, *J. Geophys. Res.*, *104*(B8), 17,661–17,674, doi:10.1029/1999JB900120.
Willenbring, J. K., and F. von Blanckenburg (2010), Long-term stability of global erosion rates and weathering during late-Cenozoic cooling, *Nature*, *465*(7295), 211–214.
Wobus, C., K. X. Whipple, E. Kirby, N. Snyder, J. Johnson, K. Spyropolou, B. Crosby, and D. Sheehan (2006), Tectonics from topography: Procedure, promise, and pitfalls, in *Tectonics, Climate and Landscape Evolution*, edited by S. Willet et al., *Geol. Soc. Am. Spec. Pap.*, 398, 55–74.
Wulf, H., B. Bookhagen, and D. Scherler (2010), Seasonal precipitation gradients and their impact on fluvial sediment flux in the Northwest Himalaya, *Geomorphology*, *118*(1–2), 13–21.

Wulf, H., B. Bookhagen, and D. Scherler (2012), Climatic and geologic controls on suspended sediment flux in the Sutlej River Valley, Western Himalaya, *Hydrol. Earth Syst. Sci.*, *16*(7), 2193–2217.
Yanites, B. J., G. E. Tucker, and R. S. Anderson (2009), Numerical and analytical models of cosmogenic radionuclide dynamics in landslide-dominated drainage basins, *J. Geophys. Res.*, *114*, F01007, doi:10.1029/2008JF001088.
Yanites, B. J., G. E. Tucker, K. J. Mueller, Y.-G. Chen, T. Wilcox, S.-Y. Huang, and K.-W. Shi (2010), Incision and channel morphology across active structures along the Peikang River, central Taiwan: Implications for the importance of channel width, *Geol. Soc. Am. Bull.*, *122*(7–8), 1192–1208.
Zhisheng, A., et al. (2011), Glacial-interglacial Indian summer monsoon dynamics, *Science*, *333*(6043), 719–723.